

# Experimental study on the coherent structure of turbulent open-channel flow using visualization and picture processing

By TADASHI UTAMI AND TETSUO UENO

Ujigawa Hydraulic Laboratory, Disaster Prevention Research Institute, Kyoto University,  
Yoko-Ohji, Fushimi-Ku, Kyoto, 612 Japan

(Received 13 December 1984 and in revised form 12 June 1986)

Coherent structures of turbulent open-channel flow in the wall region of a channel bed were examined quantitatively using experimental data obtained by flow visualization. Successive pictures of flow patterns in two horizontal cross-sections at different levels near the channel bed were taken, and then were digitized and analysed by a computer.

This method of flow visualization and picture processing enabled us to calculate the distributions of the three components of the velocity vectors. The distributions of velocities, streamlines, two-dimensional divergence and three components of vorticity could be calculated and are displayed as graphical output. In our numerical analyses, the idea of a two-dimensional correlation coefficient is introduced, through which the degree of similarity of turbulence structures can be better estimated than with the usual one-dimensional coefficient. Use of the data was based on the premise that the essential element in a turbulence structure is vortex motion.

We propose a conceptual model of turbulence structure in which the elementary unit of coherent structure in the buffer layer is presumed to be a horseshoe vortex and in which the characteristics of the multiple structure of turbulence are shown with respect to the scale, arrangement and generating process of horseshoe vortices and longitudinal vortices. Our model clearly explains the generating mechanism and mutual relations of low-speed regions, high-speed regions, ejections, sweeps and localized free-shear layers.

---

## 1. Introduction

Experimental research on turbulence structures has been conducted since the 1940s. In the 1960s, the development of measuring techniques with hot-wire velocimeters and of analysing techniques that use electronic calculators clarified various statistical properties of turbulence structures.

Kline & Runstadler (1959) and Kline *et al.* (1967) showed using flow visualization that the flow structure in the boundary layer is not as disordered as had been previously supposed. Corino & Brodkey (1969) made detailed observations of flow events containing ejections and sweeps in the wall region of pipe flows. Prior to those studies, Hama (see Corrsin 1957) had observed a streamwise streaky structure at the wall in a turbulent shear flow.

After these enlightening studies, various flow-visualization methods were developed that showed the coherent structure of a turbulent flow. In addition, probe measurements, in which new techniques such as conditional sampling were introduced, contributed to the progress made in this field.

Review articles describing the development of this research have been published by Laufer (1975) and Willmarth (1975), and Cantwell (1981) has recently published an extensive, up-to-date detailed review. These authors also suggested the future direction that research should take. A review of the published research and our previous publications (Utami & Ueno 1979, 1984) have convinced us that the elementary unit of coherent structure in a turbulent flow is vortex motion. A structural model based on the concept of a horseshoe vortex was presented by Theodorsen (1955) to account for the generating process of turbulence. In the model he included the characteristics of the multiple structure of turbulence developed by Richardson and others who had done research on similarity laws.

Since then several analogous models have been proposed, and the existence and characteristics of the vortical structure have been discussed. Recently, Head & Bandyopadhyay (1981) visualized the cross-section of a boundary-layer flow using a sheet of laser light. They observed various cross-sections of vortices and suggested that hairpin or horseshoe vortices exist. Their conceptual model indicates more clearly the characteristics of the double structure of vortical motion. Moin & Kim (1985) used a large-eddy-simulation technique to investigate the existence of hairpin vortices in a turbulent flow.

Measuring techniques have developed along with the conceptual image of a turbulence structure, as has the hardware used to make measurements. Kline (1978) summarized the advantages and disadvantages of using visual or probe methods. He reported that by using the visual method we can easily survey an entire flow field and can understand phase relations for a turbulence structure over time and space, whereas it is difficult to obtain exact, quantitative data by visualization methods. In a conclusion, he recommended the simultaneous use of two methods as reported by Offen & Kline (1973), Falco (1977) and Head & Bandyopadhyay (1978).

The recent, remarkable progress in the use of computer techniques has enabled us to process large numbers of pictures rapidly and in detail and to display the results. Kinoshita (1981) used two cameras to photograph many coloured, neutral tracer particles in a flow illuminated by stroboscope light. He calculated the three-dimensional location of each particle from pairs of pictures and showed the three-dimensional distribution of velocity vectors as a bird's-eye view. Imaichi & Ohmi (1983) have developed a new system using image processing to estimate certain physical variables of two-dimensional flows. Utami & Ueno (1984) have proposed a method to obtain three-dimensional, quantitative information from a series of pictures of cross-sections of a turbulent flow, which proves the validity of and broadens the use of flow visualization.

In this paper, we first develop the method of flow visualization and picture analysis proposed by Utami & Ueno (1984). Next, we calculate and display the distributions of such hydraulic quantities and properties as the three components of velocity vectors, the components of vorticity vectors, two-dimensional divergence, streamlines and correlation coefficients. Then we propose the concept of a two-dimensional correlation coefficient and show that some results obtained using the prevailing correlation-analysis method do not always reflect the true characteristic properties of turbulence structures. Lastly, we present a conceptual model of coherent structure of turbulence, in which the characteristics of the multiple structure of turbulence are proposed. Terms concerning the coherent structure of turbulence such as low-speed regions, high-speed regions, ejections, sweeps, longitudinal vortices, horseshoe vortices and localized free-shear layers are explained clearly with our model.

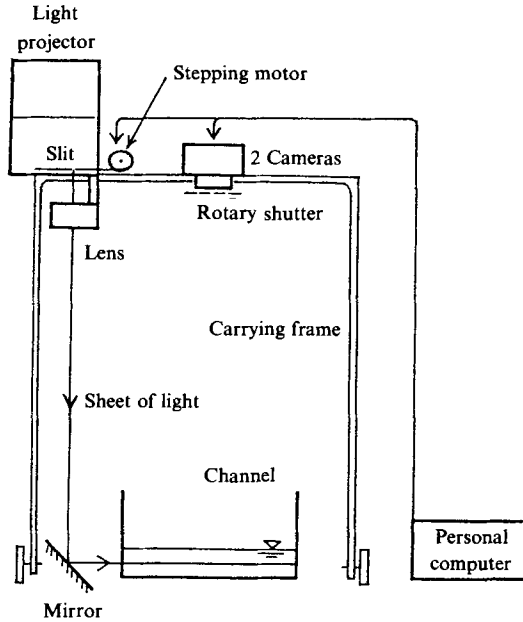


FIGURE 1. Experimental set-up.

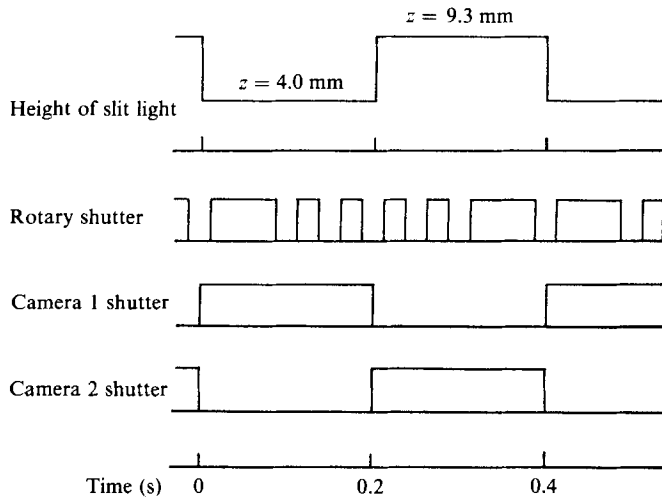


FIGURE 2. Timing of the shutter opening and illumination.

## 2. Experimental method and conditions

A tracer method was used to visualize the successive flow patterns in horizontal cross-sections of a straight open-channel flow. The experimental channel (40 cm wide) was made of clear Plexiglas to allow visualization. Polystyrene beads 0.1–0.5 mm in diameter were used as the tracers. A horizontal cross-section was illuminated by a sheet of white light passed through a thin slit attached to the illuminator (figure 1), and a picture of the flow patterns in the section was taken by one of two still cameras mounted above the channel. Immediately afterwards, the sheet of light was shifted

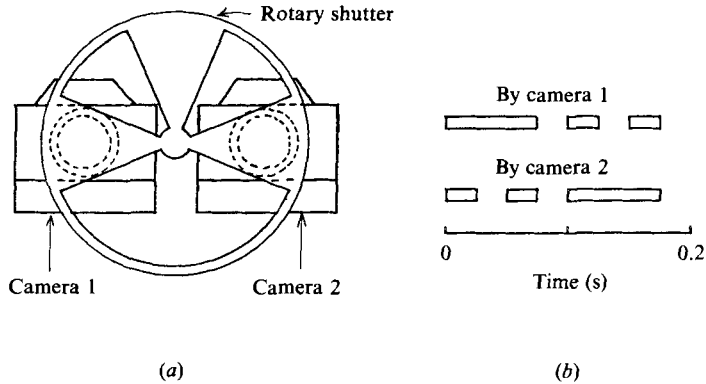


FIGURE 3. (a) Rotary shutter; (b) image of the tracer trajectory.



FIGURE 4. Picture of flow patterns in horizontal cross-section 235.

a few millimeters by moving the slit, and a picture of the flow patterns in the newly illuminated cross-section was taken by the other camera. By repeating this procedure, successive pictures of the flow patterns in horizontal cross-sections of given heights could be taken.

In order to understand experimentally the nature of turbulence, it is considered most effective to follow turbulence structures in the Lagrangian manner and to observe development of the structures, as done by Corino & Brodkey (1969) and Smith (1978). Therefore, the cameras and illuminator were mounted on the same measuring frame and moved in the flow direction at a velocity nearly equal to the

mean velocity of the flow so that the development of the same flow structures could be followed. The heights of the illuminated cross-sections, the shift distance of the section and the shutter timing were all controlled by a personal computer, and any value could be set for each one.

The experimental results obtained by alternately shifting the illuminated cross-section upward and downward every 0.2 s (figure 2) are presented and examined. The illuminated cross-section was 3 mm thick and about 9.3 or 4 mm from the channel bed. The camera shutter was open for about 0.17 s when the illuminated cross-section was stationary and was closed when it was shifting.

The two still cameras were set closely parallel on the measuring frame. The shutter of one was open when the illuminated cross-section was in the upper position, during which time the film was wound on the other camera, and vice versa when the illuminated cross-section was in the lower position. A circular disk shutter with three perforations of different size (figure 3*a*) rotated just in front of the cameras with the same shutter timing period (0.2 s) in order to mark the time on every image of the tracers' trajectories. If a tracer remained in the light all the time that the shutter was open, the image of its trajectory would have the pattern shown in figure 3(*b*). Therefore, using the time marks, we could judge how long the tracer stayed in the light and in which direction it moved.

An example of the pictures obtained is shown in figure 4. The measuring frame was moved at a velocity of 8.05 cm/s. The average water depth around the cross-section being measured was 4.0 cm, the mean velocity 6.5 cm/s, the water temperature 14.5 °C and the Reynolds number based on flow depth 2600. Friction velocity was 0.7 cm/s.

### 3. Picture analysis

#### 3.1. Digitizing pictures and interpolating

From the series of pictures obtained, six sheets (Nos 232–237) were digitized for further analysis. The pictures were enlarged as large as the original scale of the flow. The coordinates of both ends of every effective image of the tracer trajectories in the 30 × 20 cm area of each picture were digitized by manual processing using a personal computer and a digitizer. Tracer particles that came into the illuminated region after shutter opened or went out of the region before the shutter closed did not have the perfect image patterns shown in figure 3(*b*). These images were not analysed. An example of the results, obtained for cross-section 235, is shown in figure 5; in it each line segment denotes a velocity vector and the small dot the starting point of that vector.

The digitizer has a minimum resolution size of 0.1 mm, and an error of the same order can be added through manual processing. Accordingly, the total error in velocity is evaluated as 0.2 mm/0.17 s = 1.2 mm/s, which is 2% of mean velocity. Clearly, the longer the exposure time is (in this case 0.17 s), the smaller is the error. But this leads to the period over which pictures are taken becoming longer, resulting in a dilemma for the experimenter using this method.

Time and space ranges of the areas analysed in the illuminated cross-sections are shown in table 1. The  $x$ -coordinate is set in the main flow direction along the side-wall of the channel, the  $y$ -coordinate in the horizontal and cross-flow direction, and the  $z$ -coordinate in the upward direction. The  $x$ -,  $y$ - and  $z$ -components of the velocity vectors are denoted by  $u$ ,  $v$  and  $w$ . Thus, the flow pattern was analysed in the area between the right-hand sidewall and the centreline of the channel. The origin of the

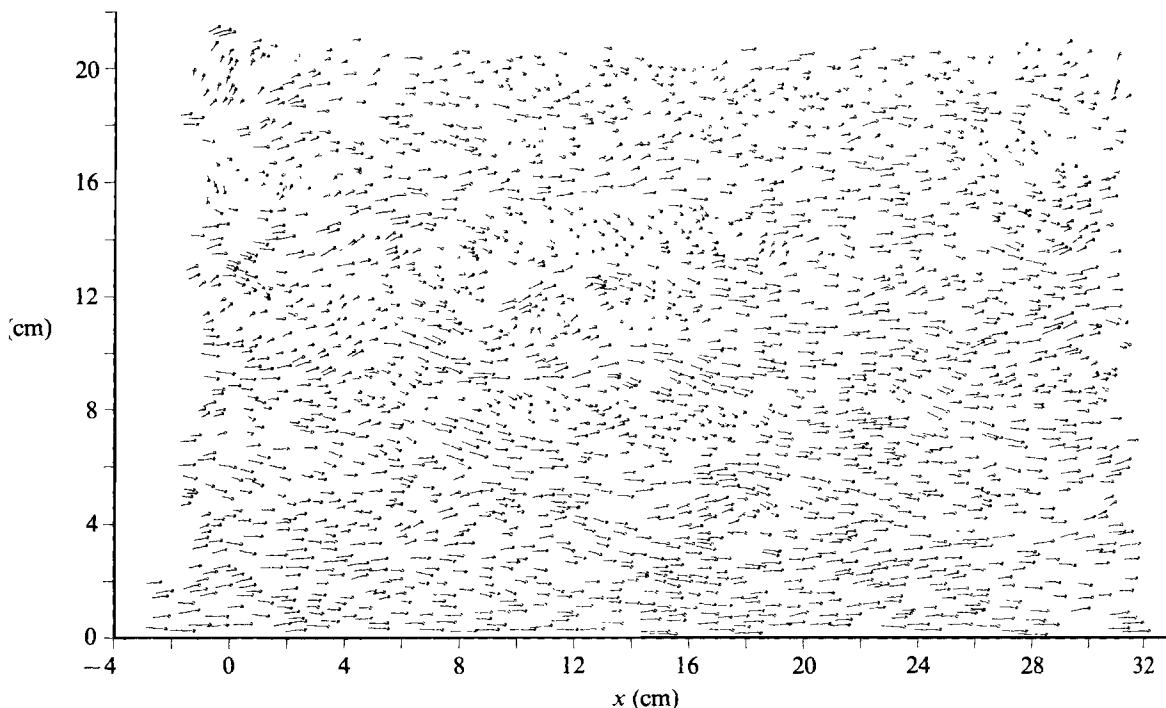


FIGURE 5. Original data on velocity vectors obtained by digitizing the picture of cross-section 235. A line segment denotes a velocity vector and a small dot the starting point.

Cross-section no.	Duration (s)	Extent		
		$x$ (mm)	$y$ (mm)	$z$ (mm)
232	0-0.173	0-300.00	0-200.00	2.5-5.5
233	0.2-0.366	12.62-312.62	0-200.00	7.8-10.8
234	0.4-0.573	25.24-325.24	0-200.00	2.5-5.5
235	0.6-0.766	37.86-337.86	0-200.00	7.8-10.8
236	0.8-0.973	50.48-350.48	0-200.00	2.5-5.5
237	1.0-1.166	63.10-363.10	0-200.00	7.8-10.8

TABLE 1. Duration and extent of the cross-sections

coordinate system for the areas analysed was shifted by 12.62 mm in the flow direction in every picture. This distance is the product of the average velocity, 6.31 cm/s, in the upper cross-section and the interval of 0.2 s between pictures.

Cross-sections with even numbers are located at the average height of 4.0 mm above the channel bed, and sections with odd numbers at the average height of 9.3 mm. The buffer layer, in this case, is about 1.0-5.0 mm above the channel bed. Accordingly, the two heights of the cross-sections are just inside and outside this layer.

For convenient data-processing later, a method of interpolation was used to obtain velocity vectors at every mesh point with an interval of 4 mm in both the  $x$ - and  $y$ -directions. For example, the distribution of the interpolated velocity vectors in

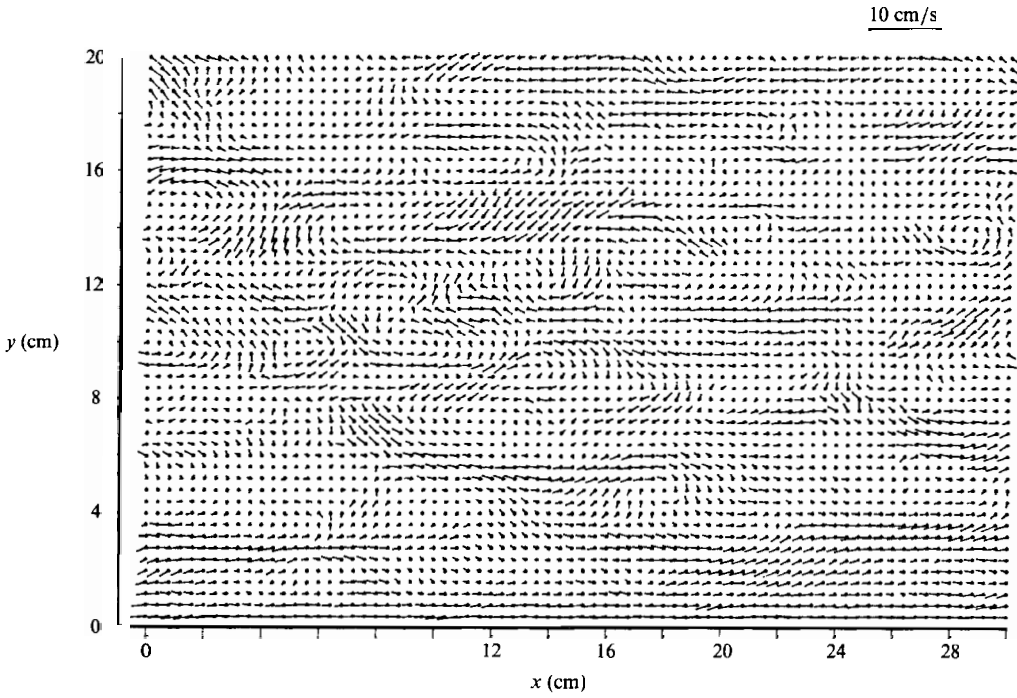


FIGURE 6. Distribution of velocity vectors at mesh points obtained by interpolating the data from figure 5 (cross-section 235).

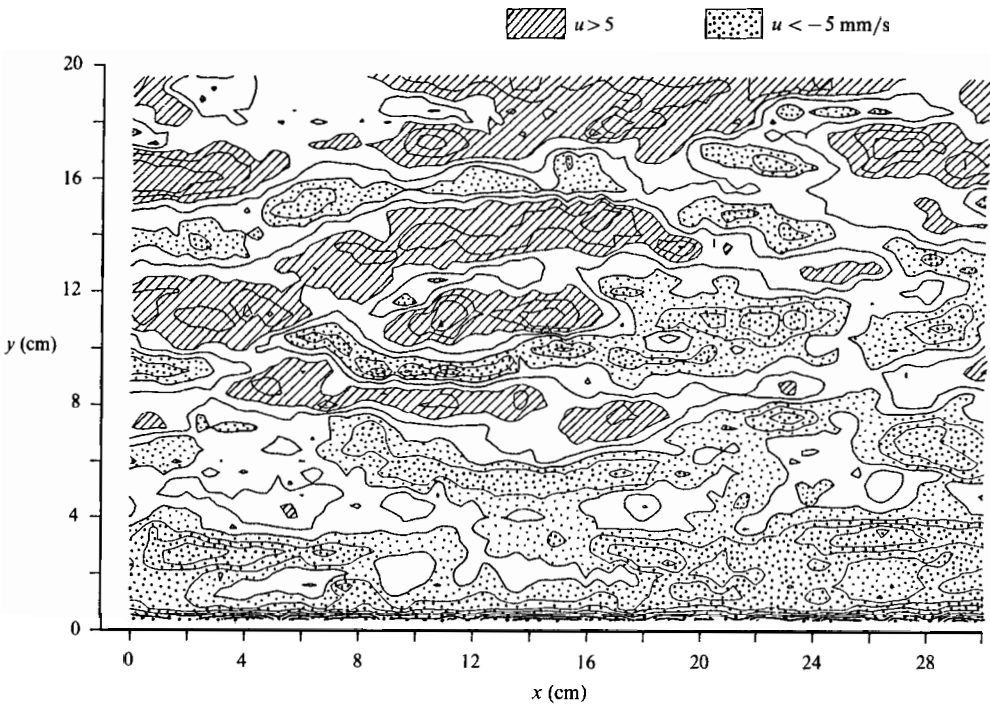


FIGURE 7. Distribution of the streamwise component of velocity vectors (cross-section 235).

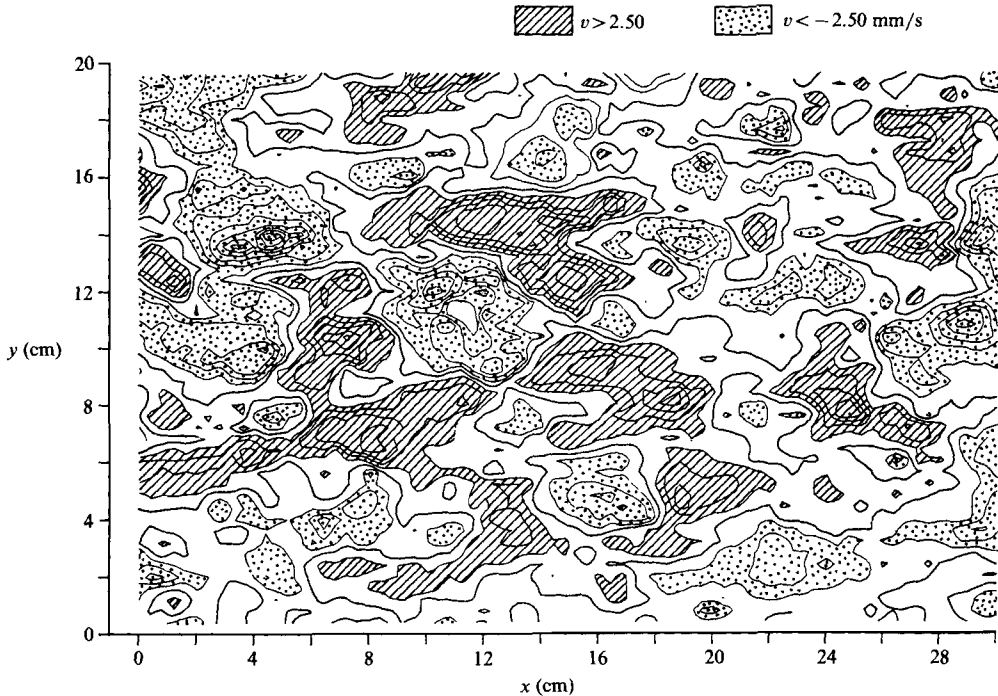


FIGURE 8. Distribution of the spanwise components of velocity vectors (cross-section 235).

cross-section 235, in which the average streamwise velocity in the cross-section has been subtracted from each vector, is shown in figure 6. This figure gives the velocity field viewed by the observer moving at the average velocity of the cross-section.

### 3.2. Velocity distributions

Distributions of the  $x$ - and  $y$ -components ( $u$  and  $v$ ) of the velocity vectors in cross-section 235 are shown in figures 7 and 8. As in figure 6, the  $x$ -component,  $u$ , represents the velocity from which the average velocity was subtracted. In figure 7, bands of low-speed and high-speed regions stretching in the flow direction alternate in the cross-flow direction. The average width of these regions is nearly equal to  $100 \nu/u_*$ .

Kline & Falco (1980) defined a streak as a high- or low-speed (relative to the mean) region in the linear sublayer, which is highly extended in the flow direction. They also defined low-speed lifting as the outward movement of fluid in the low-speed streak to a point outside the linear sublayer. In our experiments, narrowband regions in which the flow velocity is lower than the mean are present in the sublayer, buffer layer and log region. Therefore, we call such regions low-speed regions, the upward movement of flow being particularly remarkable in the buffer layer and log region. We also observed a region in which flow is high speed relative to the mean and the flow direction tends to be downward; this we call the high-speed region.

Interestingly, in figure 8 there is no pattern for the distribution of  $v$  that reflects the existence of low-speed regions; also, the longitudinal scale of each structure appears to be smaller than that of  $u$  in figure 7.

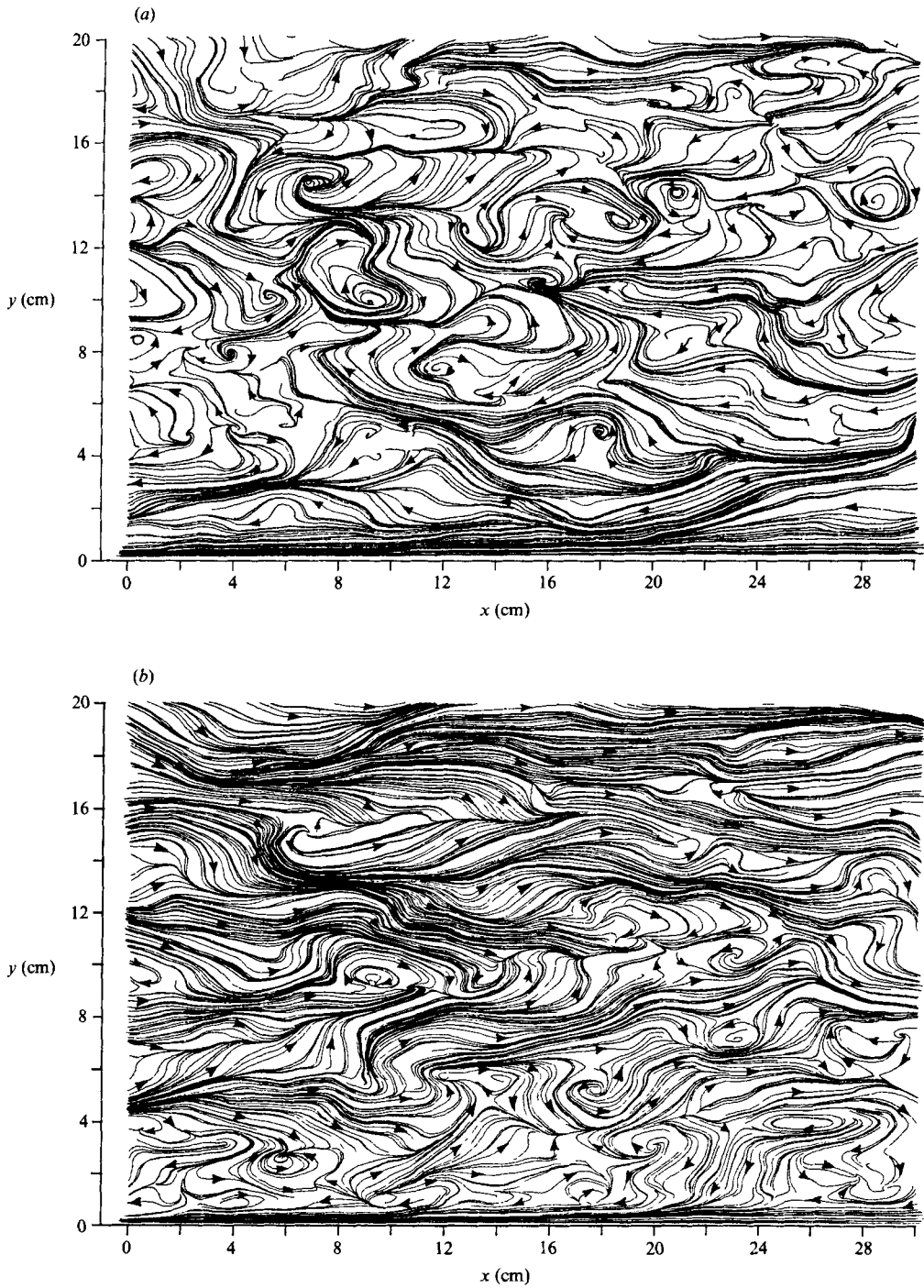


FIGURE 9. Streamline patterns viewed by the moving reference frame (cross-section 235).  
(a) Reference frame at the average velocity of the flow; (b) 1 cm/s slower.

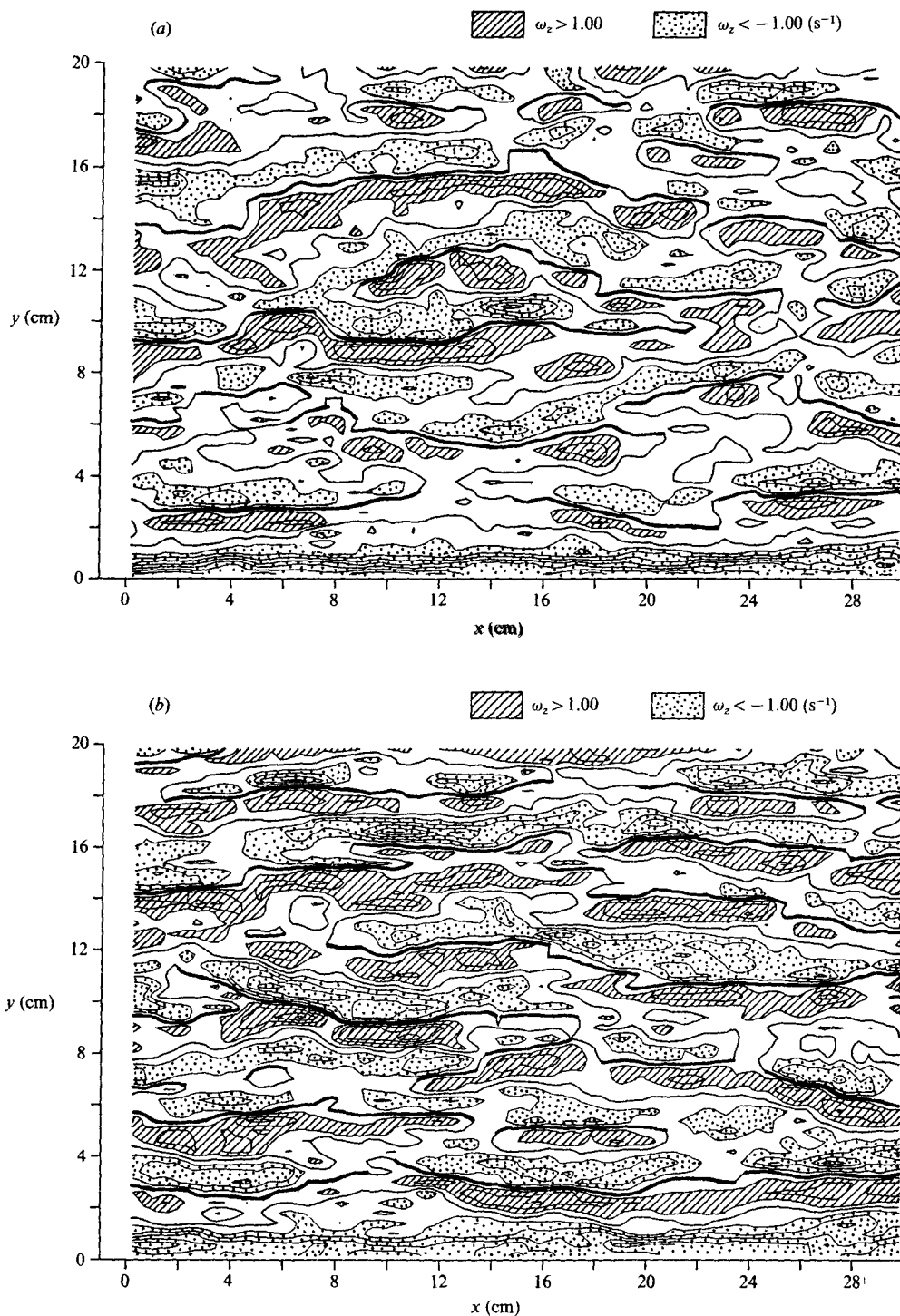


FIGURE 10. Distribution of the vertical component of vorticity (a) Cross-section 235; (b) cross-section 234.

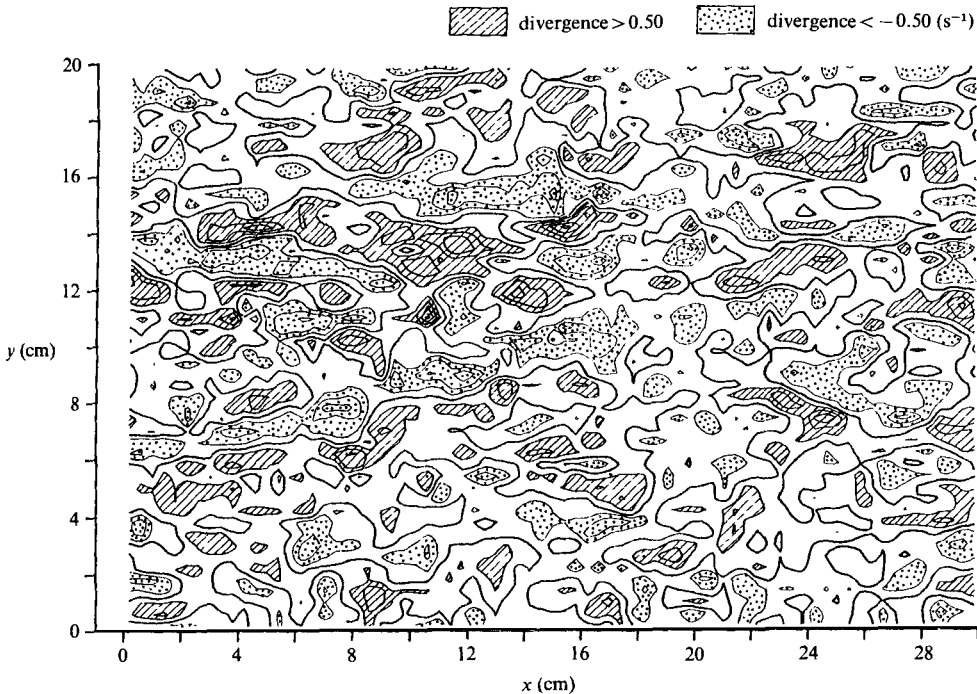


FIGURE 11. Distribution of two-dimensional divergence (cross-section 235).

### 3.3. Patterns of streamlines

Figure 9 shows patterns of streamlines in cross-section 235, obtained by drawing smooth curves tangential to each velocity vector. The patterns of streamlines are known to vary with the velocity of the observer. In this figure two patterns are given; one from a reference frame moving at the mean velocity of the flow, the other from a frame with a 1 cm/s slower velocity. Several characteristic patterns of streamlines are clear: the forming of vortex motions, converging, diverging and long stretching in a positive  $x$ - or negative  $x$ -direction. Streamlines diverging in the positive  $x$ -direction in figure 9 are present in the high-speed region of figure 7, which suggests the existence of downward flow in the region. The streamlines converging in the negative  $x$ -direction are present in the low-speed region, suggesting the existence of upward flow in the region.

### 3.4. Distribution of vorticity and divergence

Using the data for the distribution of velocity vectors shown in figure 6, we calculated the distribution of the  $z$ -components of vorticity,  $(\partial u/\partial y) - (\partial v/\partial x)$ , in cross-sections 235 and 234 which are respectively at the heights of 9.3 mm and 4 mm from the channel bed, shown in figures 10(a, b). In this calculation the differences,  $dx$  and  $dy$ , are taken as 4 mm and the maximum error of velocity is 1.2 mm/s stated above. Accordingly, the probable maximum error of the vertical component of vorticity is  $0.3 \text{ s}^{-1}$ .

The absolute vorticity value is high where the vortex-motion flow patterns in figure 9 occur. Accordingly, regions with large, absolute vorticity values are believed to correspond to the cross-sections of vortex motions such as in the horseshoe vortex.

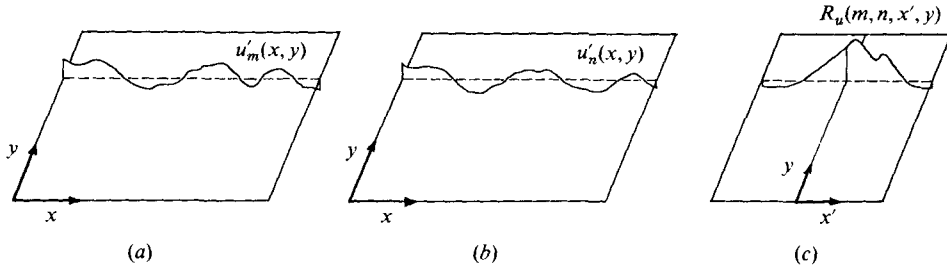


FIGURE 12. Definition sketch for the calculation of the cross-correlation coefficient. (a) Distribution of  $u'_m(x, y)$  in cross-section  $m$ ; (b) distribution of  $u'_n(x, y)$  in cross-section  $n$ ; (c) distribution of  $R_u(m, n, x', y)$ .

The existence of similar patterns in both cross-sections suggests that they are the upper and lower cross-sections of the same vortex motion.

Using the data for the distribution of velocity vectors, we calculated the distribution of two-dimensional divergence  $(\partial u/\partial x) + (\partial v/\partial y)$ , displayed in figure 11. Similar error estimation with that of vorticity is applicable and the probable maximum error is  $0.3 \text{ s}^{-1}$ . The divergence value is low where there are converging streamline patterns in figures 9(a, b), and high where there are diverging ones.

#### 4. Two-dimensional display of correlation coefficients

##### 4.1. One-dimensional cross-correlation coefficients

Cross-correlation coefficients were examined for the distribution of the velocity component  $u$  along the line  $y = y$  in one cross-section and along the same line,  $y = y$  in another cross-section.

The velocity at point  $(x, y)$  in cross-section  $m$  is denoted by  $u_m(x, y)$  and that in cross-section  $n$  by  $u_n(x, y)$ . Then the fluctuating components of velocity  $u$  along line  $y = y$  can be written

$$u'_m(x, y) = u_m(x, y) - \frac{1}{L} \int_0^L u_m(x, y) dx, \quad \text{in cross-section } m, \quad (1)$$

$$u'_n(x, y) = u_n(x, y) - \frac{1}{L} \int_0^L u_n(x, y) dx, \quad \text{in cross-section } n, \quad (2)$$

where  $L$  is the lengthscale of analysis in the  $x$ -direction; in this case 30 cm.

The cross-correlation function  $C_u(m, n, x', y)$  is defined as

$$C_u(m, n, x', y) = \int_0^{L-x'} \frac{u'_m(x, y) u'_n(x+x', y) dx}{L-x'}, \quad \text{when } x' \geq 0, \quad (3)$$

$$C_u(m, n, x', y) = \int_0^{L+x'} \frac{u'_m(x-x', y) u'_n(x, y) dx}{L+x'}, \quad \text{when } x' < 0, \quad (4)$$

where  $x'$  is the shift distance, and the cross-correlation coefficient  $R_u(m, n, x', y)$  is defined as

$$R_u(m, n, x', y) = C_u(m, n, x', y) / \left[ \frac{1}{L} \int_0^L \{u'_m(x, y)\}^2 dx \frac{1}{L} \int_0^L \{u'_n(x, y)\}^2 dx \right]^{1/2}. \quad (5)$$

The definition sketch of  $R_u(m, n, x', y)$  is given in figure 12.

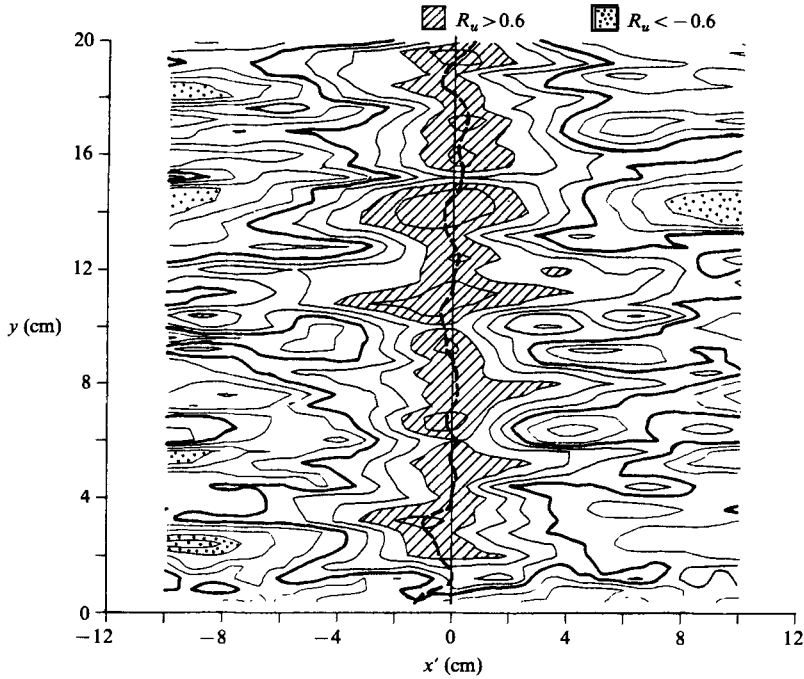


FIGURE 13. Distribution of  $R_u(233, 235, x', y)$  of the velocity component  $u$  between cross-sections 233 and 235.

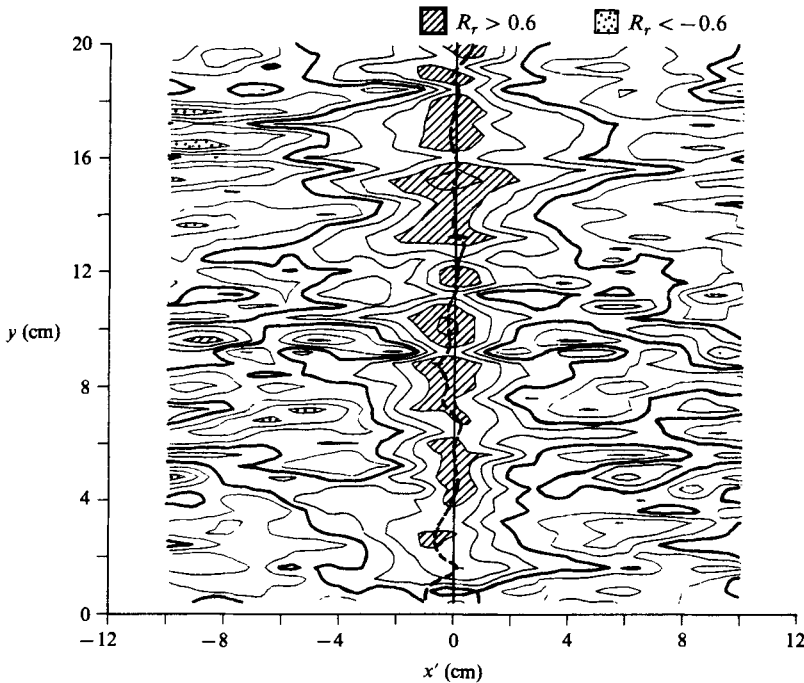


FIGURE 14. Distribution of  $R_v(233, 235, x', y)$  of the vertical component of vorticity between cross-sections 233 and 235.

The two-dimensional distribution of the cross-correlation coefficient  $R_u(233, 235, x', y)$  between cross-sections 233 and 235, both located in the upper cross-section, was calculated and is displayed in figure 13. The time lag between these two cross-sections is 0.4 s. The ridge line of the contours of the cross-correlation coefficient is shown by broken line. The bold, solid lines are contours on which  $R_u(233, 235, x', y)$  equals zero.

The cross-correlation coefficients of the distributions of the  $z$ -component of vorticity  $R_r(233, 235, x', y)$  in these cross-sections were calculated in the same way, and distribution being shown in figure 14. The values for the cross-correlation coefficient of this figure are less than those of the velocity  $u$ .

If the distribution of the cross-correlation coefficient of  $u$  around the  $x' = 0$  line in figure 13 is compared with that of the vorticity around the  $x' = 0$  line in figure 14, the value of the cross-correlation coefficient of  $u$  is seen to be relatively small at locations where that value of the vorticity is large, and vice versa. But, the organized part of the turbulence structure must have a large correlation coefficient in either case when it is calculated using velocity or vorticity.

The two-dimensional  $u$ -distribution (figure 7) has a characteristic pattern composed of narrow longitudinal low-speed and high-speed regions arranged alternately in the cross-flow direction. The two-dimensional vorticity distribution (figure 10) has a similar pattern to that of  $u$ . But it should be noted that the  $z$ -component of vorticity generally has a large absolute value in areas in which the absolute value of  $u$  is small and vice versa. With this characteristic distribution of  $u$ , the vertical component of vorticity is highly dependent on  $\partial u / \partial y$ , which has a large absolute value in areas of small absolute value of  $u$ . That is the reason for the existence of a phase lag between the  $u$ - and vorticity distributions.

The correlation coefficient obtained from data of  $u$  or vorticity over a short period is affected by these distribution characteristics. Generally, the correlation coefficient calculated from (1)–(5) tends to have a small absolute value when the  $u$ - or vorticity variation has many zero-crossing points. In areas of small absolute value of  $u$ , the  $u$ -variation has many zero-crossing points along the  $y = y$  line and the vorticity variation has a large absolute value and less zero-crossing points, which results in small  $R_u$  and large  $R_r$ . That is why the correlation coefficients for  $u$  show an opposite tendency to those for vorticity. This contradiction springs from the weak point of the method of correlation processing, which occurs when it is applied to short-period data.

#### 4.2. Two-dimensional cross-correlation coefficients

To avoid the above contradiction, it is better to calculate the correlation coefficient for the distribution of velocity or vorticity in a two-dimensional area of appropriate width. A new definition of the cross-correlation coefficient between two cross-sections will be introduced, in which the correlation coefficient is calculated from data at lattice points in band regions  $2B$  wide and  $L$  long. The two-dimensional cross-correlation function,  $C_u(m, n, x', y)$  is defined as

$$C_u(m, n, x', y) = \frac{1}{2B(L-x')} \int_{y-B}^{y+B} \int_0^{L-x'} u'_m(x, y) u'_n(x+x', y) dx dy, \quad \text{when } x' \geq 0, \quad (6)$$

$$C_u(m, n, x', y) = \frac{1}{2B(L+x')} \int_{y-B}^{y+B} \int_0^{L+x'} u'_m(x-x', y) u'_n(x, y) dx dy, \quad \text{when } x' < 0, \quad (7)$$

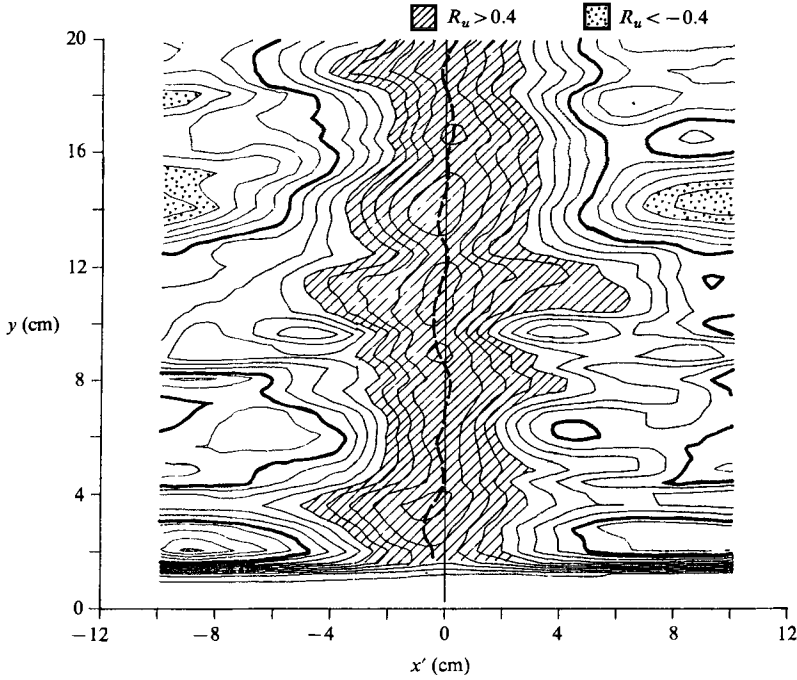


FIGURE 15. Distribution of the two-dimensional cross-correlation coefficient  $R_u(233, 235, x', y)$  of velocity component  $u$  between cross-sections 233 and 235.

where,

$$u'_m(x, y) = u_m(x, y) - \frac{1}{2BL} \int_{y-B}^{y+B} \int_0^L u_m(x, y) dx dy, \quad (8)$$

$$u'_n(x, y) = u_n(x, y) - \frac{1}{2BL} \int_{y-B}^{y+B} \int_0^L u_n(x, y) dx dy. \quad (9)$$

The two-dimensional cross-correlation coefficient  $R_u(m, n, x', y)$  is defined as

$$R_u(m, n, x', y) = \frac{C_u(m, n, x', y)}{\left[ \frac{1}{2BL} \int_{y-B}^{y+B} \int_0^L \{u'_m(x, y)\}^2 dx dy \frac{1}{2BL} \int_{y-B}^{y+B} \int_0^L \{u'_n(x, y)\}^2 dx dy \right]^{1/2}}. \quad (10)$$

In the distribution of the velocity component  $u$  (figure 7), the average width of the bands of the low-speed and high-speed regions is about 1.5–1.7 cm. Therefore, we substituted 1.6 cm for  $2B$  and 30 cm for  $L$ . The distribution of the two-dimensional cross-correlation coefficient  $R_u(233, 235, x', y)$  of the velocity  $u$  between cross-sections 233 and 235 was calculated as shown in figure 15 and the cross-correlation coefficient  $R_r(233, 235, x', y)$  of the  $z$ -component of vorticity as shown in figure 16. In these figures the bold solid lines are the contour lines on which  $R_u$  or  $R_r$  is equal to zero. The distributions obtained are not correct near the sidewall of the channel ( $y < 2$  cm).

There is no contradiction between figures 15 and 16 as there was between figures 13 and 14. Consequently, the two-dimensional cross-correlation coefficient defined by (6)–(10) is used hereafter to examine the correlation between the two cross-sections.

In figures 15 and 16, the cross-correlation coefficients  $R_u$  and  $R_r$  on the ridge line

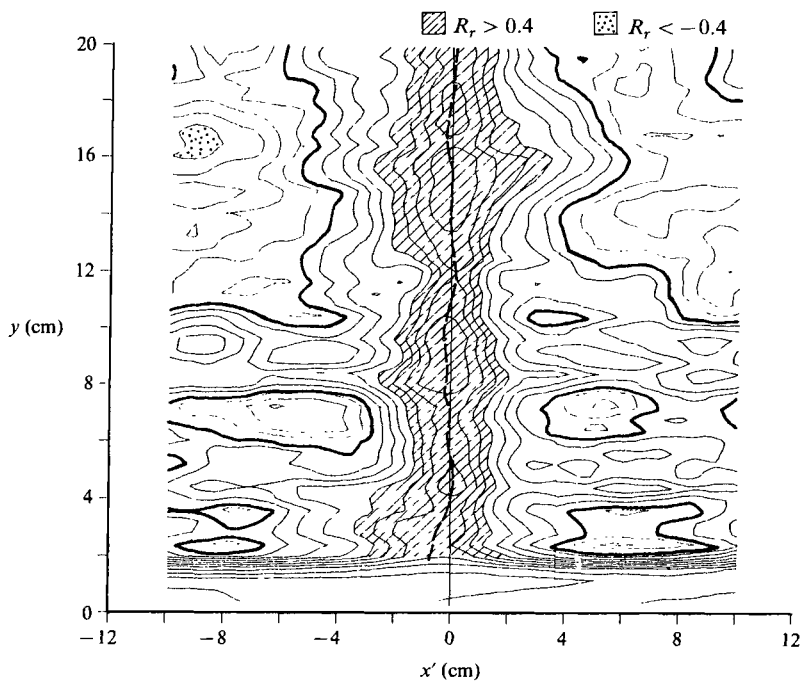


FIGURE 16. Distribution of the two-dimensional cross-correlation coefficient  $R_r(233, 235, x', y)$  of the vertical component of vorticity between cross-sections 233 and 235.

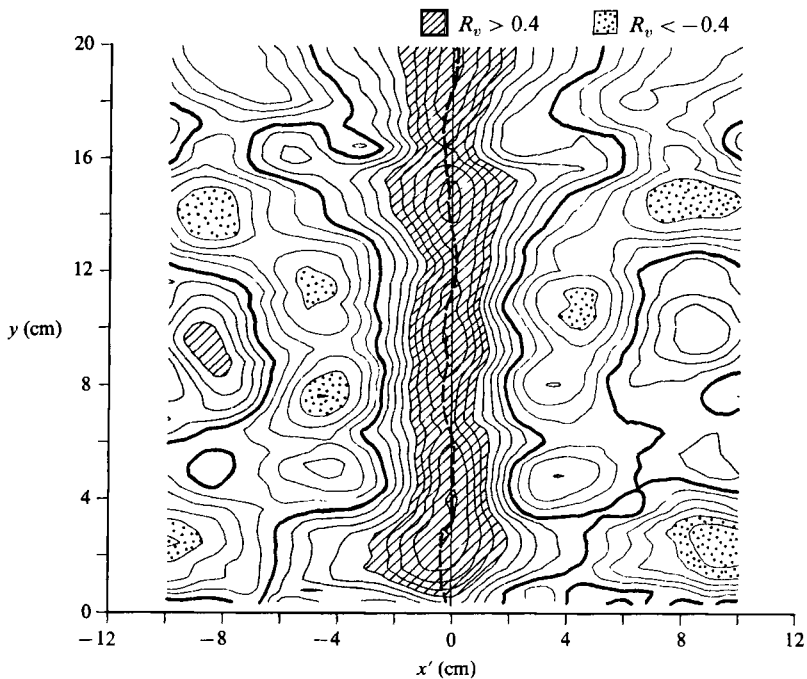


FIGURE 17. Distribution of the two-dimensional cross-correlation coefficient  $R_v(233, 235, x', y)$  of velocity component  $v$  between cross-sections 233 and 235.

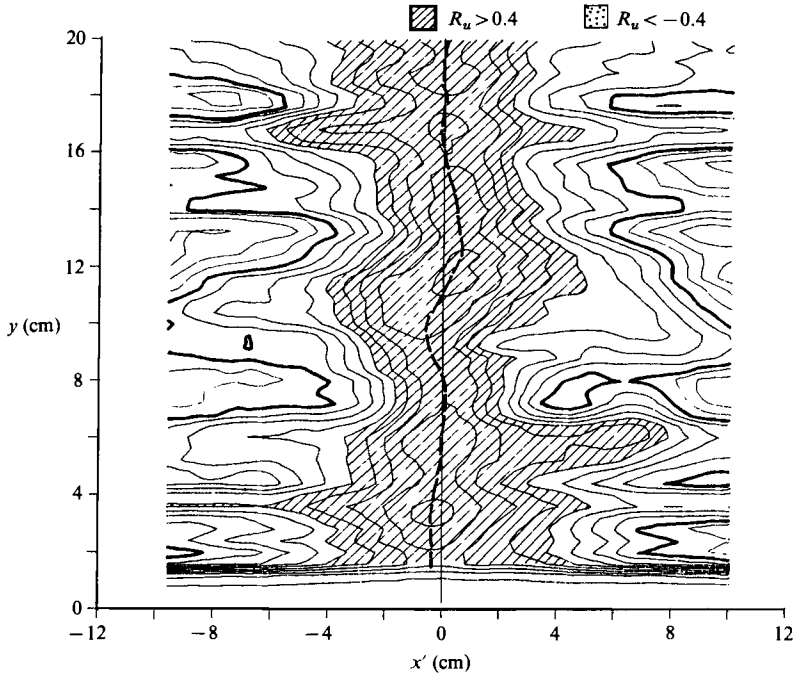


FIGURE 18. Distribution of the two-dimensional cross-correlation coefficient  $R_u(232, 234, x', y)$  of velocity component  $u$  between cross-sections 232 and 234.

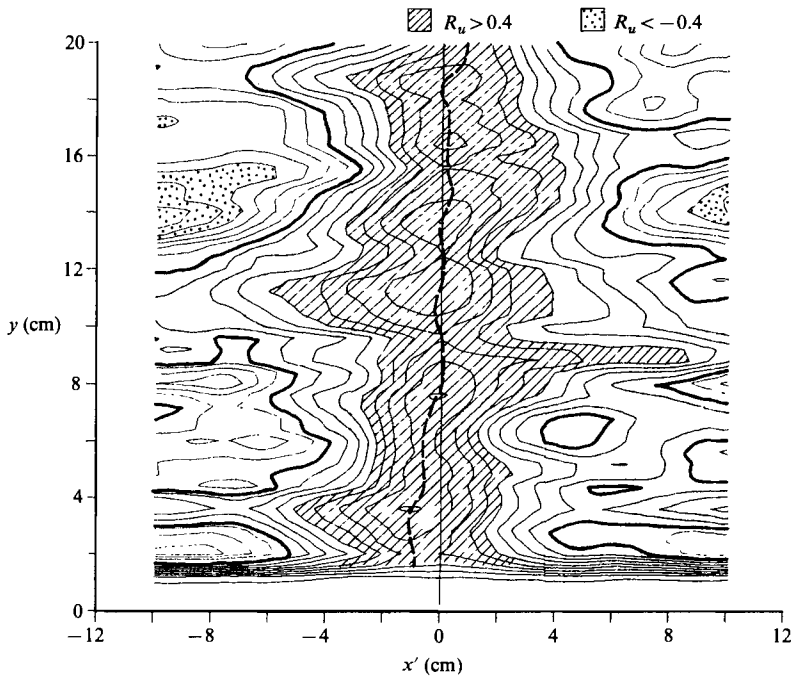


FIGURE 19. Distribution of the two-dimensional cross-correlation coefficient  $R_u(233, 237, x', y)$  of velocity component  $u$  between cross-sections 233 and 237.

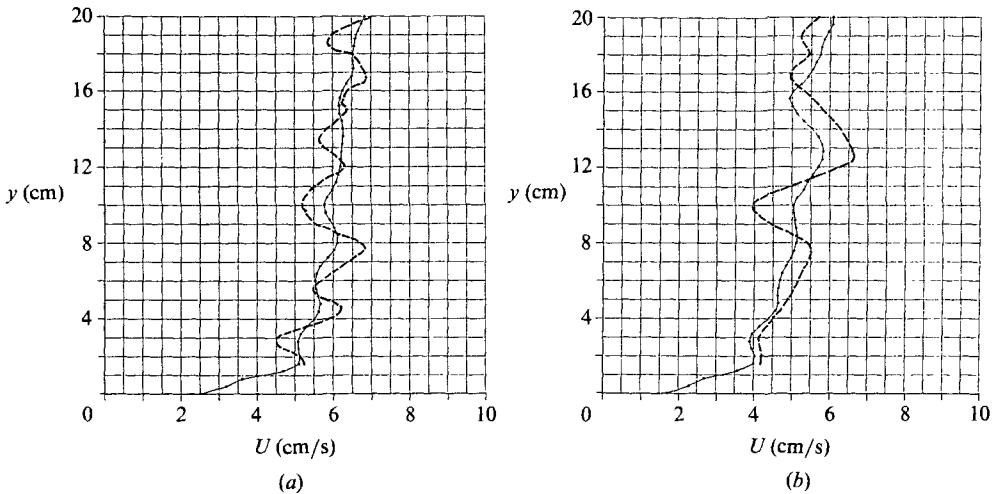


FIGURE 20. Spanwise distribution of the shifting velocity (broken line) and locally averaged streamwise velocity  $U_m(y)$  (solid line). (a) Cross-section 235; (b) cross-section 234.

are larger than 0.7 and 0.6 respectively, which means that turbulent structures remain unchanged for a short period (0.4 s). In particular, the large value for the cross-correlation coefficient of vorticity means that the magnitude and arrangement of the vortex motions are maintained with little change.

The ridge line for the distribution of the correlation coefficient is shown by the broken line in figures 15 and 16. In these figures displaying the distribution of the correlation coefficient, the origins of coordinates are set so that phase lag is equal to zero when turbulence structures are convected by the mean velocity in the cross-section. Therefore, in the area where the ridge line is on the right-hand side of the  $x' = 0$  line, turbulence structures are convected at a larger velocity than the average velocity, and in the area where the ridge line is on the left, at a smaller velocity.

The distribution of the cross-correlation coefficient  $R_v(233, 235, x', y)$  of the velocity component  $v$  between the two cross-sections is shown in figure 17. The streamwise width of the band region where  $R_v$  is positive is less than in figure 15. This is believed to be due to the difference in longitudinal scales for the velocity components  $u$  and  $v$ .

The distribution of the cross-correlation coefficient  $R_u(232, 234, x', y)$  of the velocity component  $u$  between cross-sections 232 and 234, both of which are located in the lower cross-section ( $z = 4$  mm), is shown in figure 18. The cross-correlation coefficients  $R_u$  on the ridge line are larger than 0.6. Figure 19 shows the distribution of the cross-correlation coefficient  $R_u(233, 237, x', y)$  of  $u$  between cross-sections 233 and 237, both of which are located in the upper cross-section. The time lag between these two cross-sections is 0.8 s. Even in this case, the value of  $R_u$  on the ridge line is larger than 0.5.

From these results, we conclude that the turbulence structure in the horizontal cross-section of the flow is convected downstream without large deformation over a short period.

#### 4.3. Shifting velocity of the turbulence structure

The ridge line of the distribution of the cross-correlation coefficient  $R_u(233, 235, x', y)$  is shown by a broken line in figure 15, which denotes the spanwise distribution of

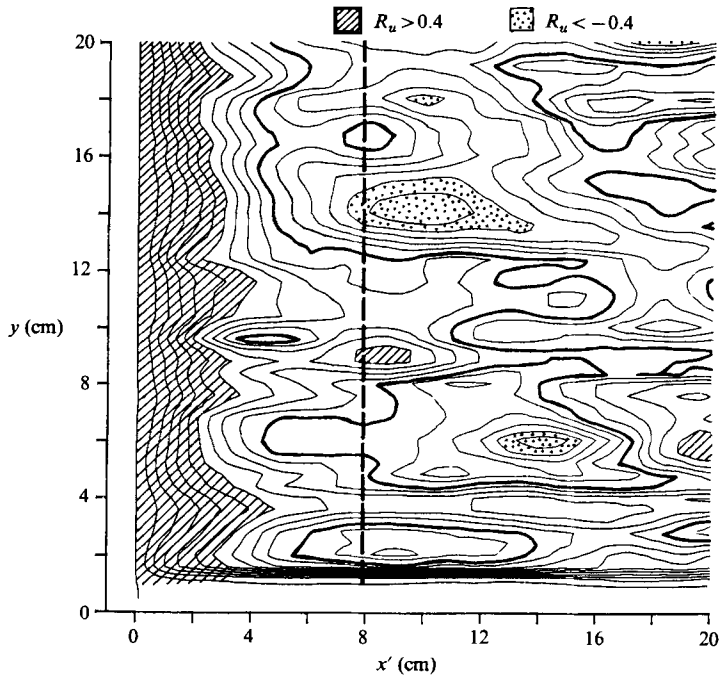


FIGURE 21. Distribution of the two-dimensional autocorrelation coefficient  $R_u(235, 235, x', y)$  of velocity component  $u$  (cross-section 235).

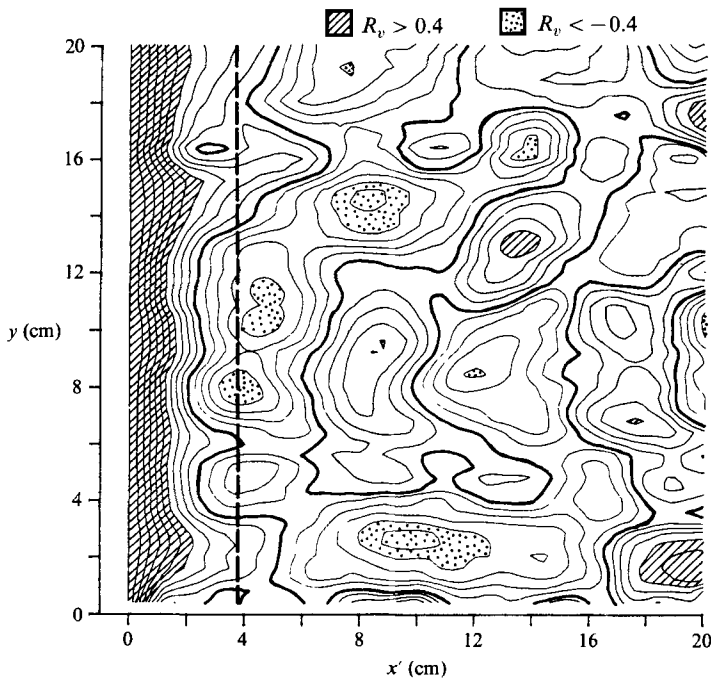


FIGURE 22. Distribution of the two-dimensional autocorrelation coefficient  $R_v(235, 235, x', y)$  of velocity component  $v$  (cross-section 235).

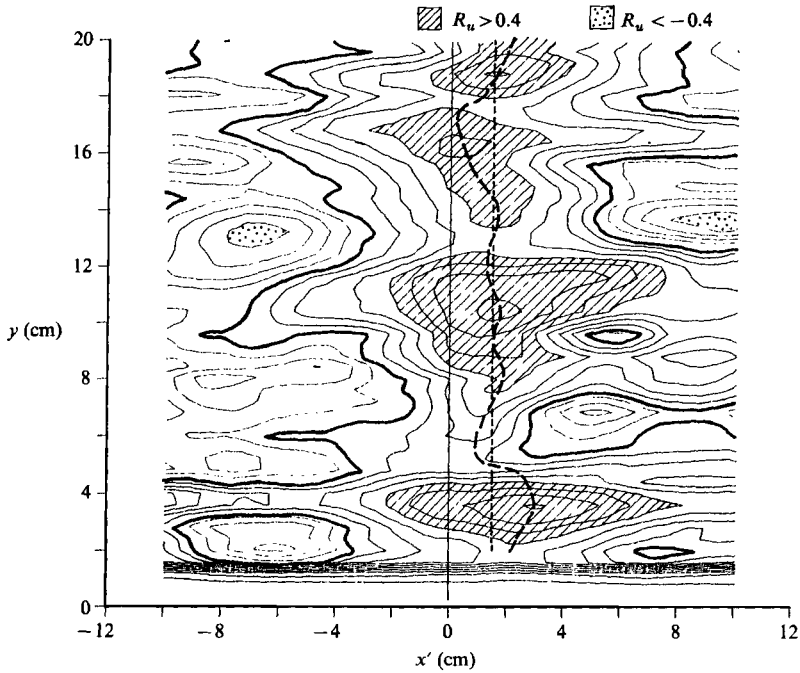


FIGURE 23. Distribution of the two-dimensional cross-correlation coefficient  $R_u(234, 235, x', y)$  of velocity component  $u$  between cross-sections 234 and 235.

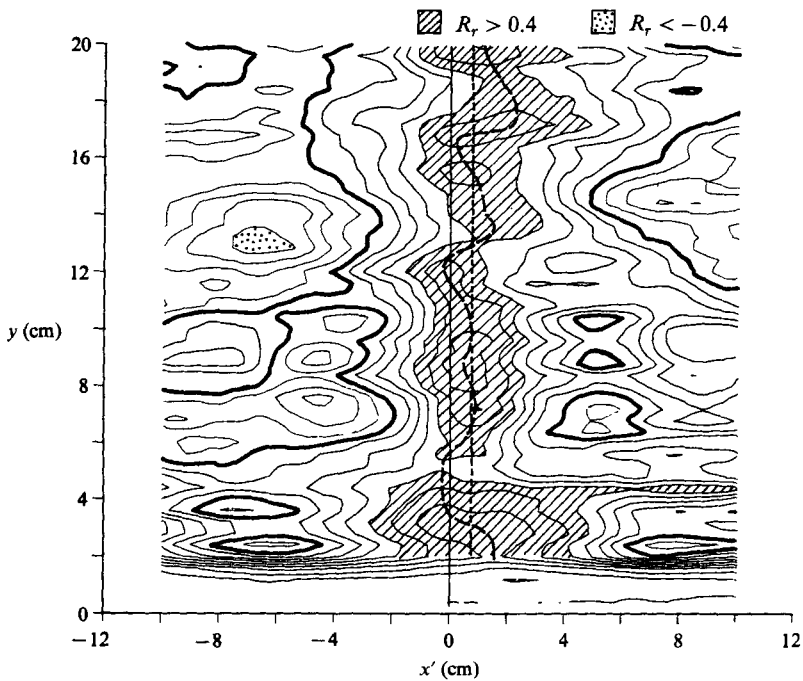


FIGURE 24. Distribution of the two-dimensional cross-correlation coefficient  $R_r(234, 235, x', y)$  of the vertical component of vorticity between cross-sections 234 and 235.

the phase-lag distance of the  $u$ -distribution between cross-sections 233 and 235. The spanwise distribution of the local shifting velocity of turbulence structures is calculated from the phase-lag distance and is shown by the broken line in figure 20.

By contrast, the distribution of the locally averaged streamwise velocity  $U_m(y)$  is calculated as

$$U_m(y) = \frac{1}{2BL} \int_{y-B}^{y+B} \int_0^L u(x, y) dx dy, \quad (11)$$

where,  $B = 0.8$  cm and  $L = 30$  cm. The distribution of  $U_m(y)$  obtained in cross-section 235 is shown by the solid line in figure 20(a).

Distributions of the shifting velocity calculated as above for cross-sections 232 and 234, and locally averaged streamwise velocities for cross-section 234 are shown in figure 20(b). The distributions of the two kinds of velocities have wavy patterns, both having nearly equal local means and configurations of nearly equal phase.

Therefore, we hypothesize that the structure of turbulence is frozen and convected at the local averaged velocity given by (11).

#### 4.4. Autocorrelation coefficients of velocity distributions

It is suggested above that the longitudinal scale of the velocity component  $u$  differs from that of  $v$ . Therefore, we calculated the autocorrelation coefficients of  $u$  and  $v$  in order to examine their scales.

The autocorrelation coefficient is defined by (6)–(10) in which  $n$  is substituted by  $m$ . The distributions of autocorrelation coefficients  $R_u(235, 235, x', y)$  for  $u$ -fluctuations and  $R_v(235, 235, x', y)$  for  $v$ -fluctuations in cross-section 235 are shown in figures 21 and 22, in which the average  $x'$ -coordinates of the location of the downward zero-crossing of the autocorrelation coefficients are shown by broken lines. The value for the autocorrelation of  $u$  is 7.9 cm and that of  $v$ , 3.7 cm, which means that the longitudinal scale of  $u$  is approximately twice that of  $v$ .

#### 4.5. Inclination of turbulence structures

The distribution of the cross-correlation coefficient  $R_u(234, 235, x', y)$  of  $u$  between lower cross-section 234 and upper cross-section 235 is shown in figure 23. The time lag between the two is 0.2 s. The origins of coordinates are set so that phase lag is equal to zero when turbulence structures are convected by the mean velocity in the cross-section. The ridge line of the distribution of the correlation coefficient is shown by a broken line, and its average  $x'$ -coordinate by a dotted line. It should be noted that some phase lag exists throughout the width of the flow. The lag distance is believed to be due to the inclination of the turbulence structures, the average value being 15.2 mm and the angle of phase lag calculated from this value is 19.2°. This angle is nearly equal to that measured by Brown & Thomas (1977), Kreplin & Eckelmann (1979), Nakagawa & Nezu (1981) and Ohnari, Saga & Saito (1985).

The distribution of the cross-correlation coefficient  $R_r(234, 235, x', y)$  of the  $z$ -component of vorticity between cross-sections 234 and 235 is shown in figure 24. The ridge line and the average line also are shown. The average value for phase-lag distance is 7.3 mm and the average inclination 36.0°. Note that this angle is twice as large as the angle inclination obtained from the velocity correlation analysis.

## 5. Three-dimensional properties of velocity distributions

### 5.1. Calculation of the vertical component of velocity

As our velocity data were obtained from pictures of horizontal cross-sections of the flow, we have so far no information on the vertical components of the velocity vectors. But if a hypothesis of frozen structures of turbulence is introduced, the effect of the time lag between two pictures of different height can be removed, and it is possible to recombine the three-dimensional distributions of  $u$  and  $v$  at certain times and to calculate the vertical components of the velocity vectors using the continuity equation.

In the preceding section we concluded that turbulence structures are convected at a velocity that is obtained by averaging all the velocity components  $u$  over the band area of the velocity distribution. We assume that velocity distributions are frozen on the longitudinal line and convected at the reported velocity. The band width used for the averaging was 1.6 cm, as in the preceding section.

On our assumption, the distributions of  $u$  and  $v$  along every longitudinal line in the upper cross-section were shifted in the negative  $x$ -direction by a distance of  $U_c Dt$ ,  $U_c$  being the supposed convecting velocity and  $Dt$  the time difference (0.2 s) between the two cross-sections. Thus, the three-dimensional distributions of  $u$  and  $v$  near the channel bed at the instant the picture of the lower cross-section was taken could be obtained. The distribution of the vertical component  $w$  of a velocity vector could be obtained from numerical calculations using the continuity equation

$$w = \int_0^z dw = - \int_0^z \left( \frac{\partial u}{\partial x} + \frac{\partial v}{\partial y} \right) dz. \quad (12)$$

But information on two-dimensional divergence, which appears in parentheses on the right-hand side of (12) is limited to the horizontal cross-sections at  $z = 4$  and 9.3 mm. It is clear that two-dimensional divergence on the wall surface is zero. But the absolute value of two-dimensional divergence in the cross-section  $z = 4$  mm is generally larger than that in the cross-section  $z = 9.3$  mm, which suggests that assuming linear variation of two-dimensional divergence between the cross-sections  $z = 0$  and 4.0 mm is not suitable. Consequently, we assume that on the wall surface the two-dimensional divergence is zero, on the outer boundary of the viscous sublayer ( $z = 1$  mm) the divergence value is equal to that in the  $z = 4$  mm cross-section and that the value of two-dimensional divergence varies linearly between each cross-section. Therefore, three-dimensional distributions of the three components of the velocity vectors could be obtained every 0.4 s.

As an example, the resulting distribution of the vertical component of velocity in the cross-section at  $z = 9.3$  mm, which corresponds to the data for 235, is shown in figure 25. The calculated distributions of  $u$  and  $v$  in the upper horizontal cross-sections are almost the same as the original distribution because time passed (0.2 s) is very short; therefore they are not shown here.

The accuracy of such distributions of the vertical component of velocity is inferior to that of horizontal components because the calculation is based on the hypothesis of frozen turbulence and the approximate distribution of two-dimensional divergence.

### 5.2. Distribution of instantaneous Reynolds stress

We define ejections, sweeps and interactions after the four-quadrant method of Wallace, Eckelmann & Brodkey (1972). Areas with large positive  $w$ -values in figure

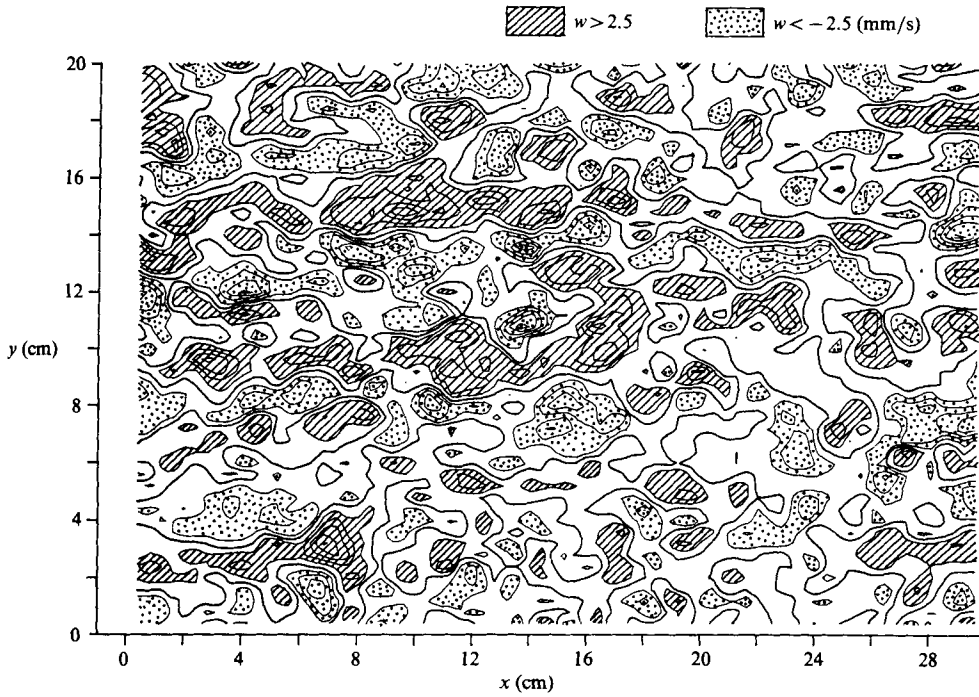


FIGURE 25. Distribution of the vertical component of velocity (cross-section 235).

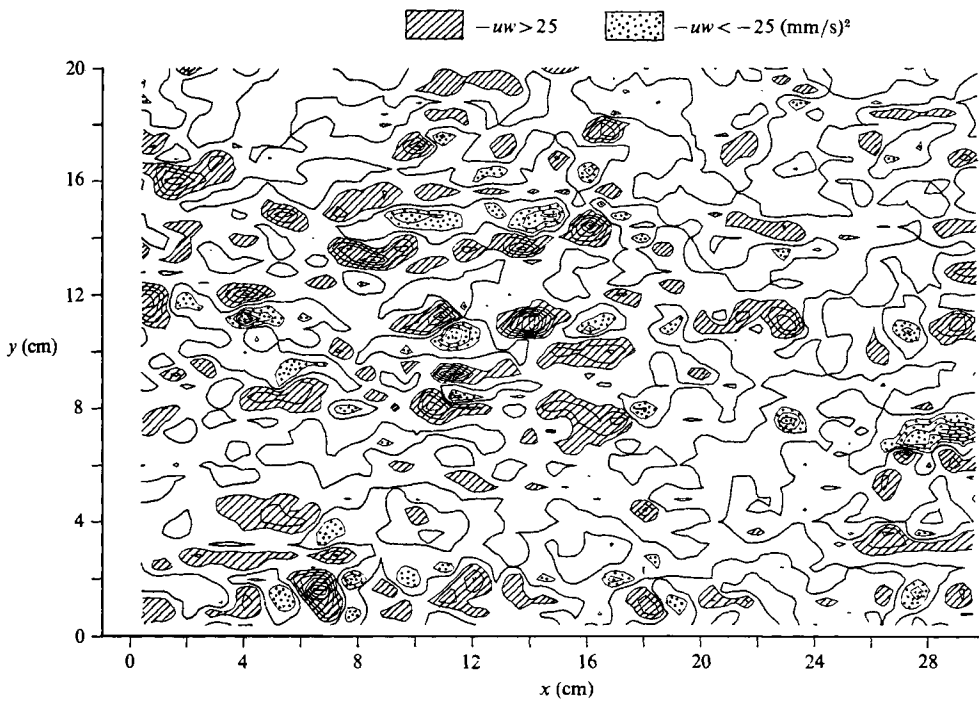


FIGURE 26. Distribution of the instantaneous Reynolds stress (cross-sections 235).

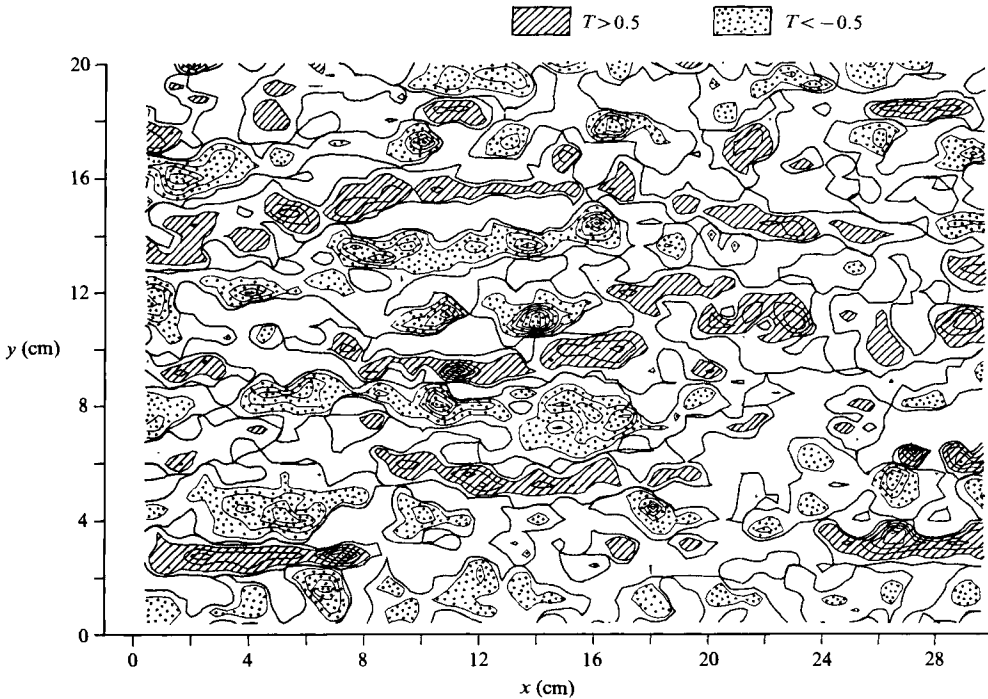


FIGURE 27. Distribution of the  $T$ -function of  $-u(x, y)$  and  $w(x, y)$  (cross-section 235).

25 nearly coincide with the areas of negative  $u$ -values in figure 7, and those of negative  $w$ -values, with those of positive  $u$ -values.

Using the three-dimensional distribution of velocity vectors we could calculate the distribution of instantaneous Reynolds stress  $-uw$ . One set of results is shown in figure 26. In the regions of positive Reynolds stress sweeps or ejections occur and in the regions of negative Reynolds stress, interactions occur. The former occupies much larger areas than the latter. This figure also shows that most of the contributions to the instantaneous Reynolds stress of large absolute value are made by sweeps or ejections; but it gives no information on the individual contributions of these ejections or sweeps.

### 5.3. Distributions of ejections and sweeps

We now introduce the  $T$ -function by which we could estimate individual contributions to Reynolds stress by ejections and sweeps. The  $T$ -function is defined as

$$T_{pq}(x, y) = p(x, y) q(x, y) \quad \text{when } p(x, y) \geq 0, \quad q(x, y) \geq 0, \quad (13)$$

$$T_{pq}(x, y) = -p(x, y) q(x, y) \quad \text{when } p(x, y) < 0, \quad q(x, y) < 0, \quad (14)$$

$$T_{pq}(x, y) = 0 \quad \text{when } p(x, y) q(x, y) \leq 0, \quad (15)$$

where,  $p(x, y)$  and  $q(x, y)$  are the two-dimensional functions of  $x$  and  $y$  normalized by their standard deviation and  $T_{pq}(x, y)$  is the  $T$ -function of  $p(x, y)$  and  $q(x, y)$ .

The functions  $-u(x, y)$  and  $w(x, y)$ , normalized using their means and standard deviations, were substituted for  $p(x, y)$  and  $q(x, y)$  to calculate the  $T$ -function  $T_{-u, w}(x, y)$ . Results for cross-section 235 are shown in figure 27. Based on the definition of the  $T$ -function, we can say that this figure shows a close correlation

between the distribution of the instantaneous value of  $-u(x, y)$  and that of  $w(x, y)$ . Moreover, in a region with positive  $T_{-u, w}(x, y)$ -values, in which  $u(x, y)$  is negative and  $w(x, y)$  positive, ejections occur; and, in a region with negative  $T_{-u, w}(x, y)$ -values, in which  $u(x, y)$  is positive and  $w(x, y)$  negative, sweeps occur. The  $T$ -function is 0 in an area of interaction. At the same time, the absolute value of the  $T$ -function is large in an area of strong ejections or sweeps.

In this calculation, the mean values  $u_m(y)$  and  $w_m(y)$  of  $u(x, y)$  and  $w(x, y)$ , and the standard deviations  $u_{\text{rms}}(y)$  and  $w_{\text{rms}}(y)$  are necessary for the normalization. Taking into account that the  $u$ -distribution is composed of narrow bands of high-speed and low-speed regions arranged alternately in the spanwise direction and that the average width of these bands is nearly 1.6 cm (about  $100 u_* / \nu$ ), we used the standard deviation and mean values of  $u(x, y)$  and  $w(x, y)$  in the band area between  $y = y - B$  and  $y = y + B$  but with  $w_m$  substituted by 0. Thus,

$$u_m(y) = \frac{1}{2BL} \int_{y-B}^{y+B} \int_0^L u(x, y) dx dy, \quad (16)$$

$$w_m(y) = 0, \quad (17)$$

$$u_{\text{rms}}(y) = \left[ \frac{1}{2BL} \int_{y-B}^{y+B} \int_0^L \{u(x, y) - u_m(y)\}^2 dx dy \right]^{1/2}, \quad (18)$$

$$w_{\text{rms}}(y) = \left[ \frac{1}{2BL} \int_{y-B}^{y+B} \int_0^L \{w(x, y)\}^2 dx dy \right]^{1/2}, \quad (19)$$

where  $B = 1.6$  cm and  $L = 30$  cm.

When figure 27 is compared with figure 7, as is necessary for the definitions of sweeps and ejections, ejections are seen in low-speed regions and sweeps in high-speed regions.

#### 5.4. Distributions of vorticity vectors

The conditional-sampling method used with the phase-averaging processing of probe data has made it possible to obtain the distribution of vorticity in some kinds of flow. Browand & Weidman (1976) gave the distribution of vorticity in a two-dimensional mixing layer. Williams, Fasel & Hama (1984) gave the three dimensional vorticity field in the boundary-layer transition process. The three-dimensional distributions of the three components of velocity that we obtained through flow visualization enabled us to calculate the distributions of the three components of vorticity in the turbulent boundary layer.

##### (i) Distribution of the vertical component of vorticity

The distributions of the vertical component of vorticity  $\omega_z$  in cross-sections 235 and 234 have been calculated and displayed in figures 10(a, b). The positive region of the distribution of the vertical component of vorticity is thought to be the horizontal cross-section of a right-side leg (facing streamward) and a negative region to be a left-side leg (facing streamward) of a pair of vortex motions. Accordingly, the zero-vorticity line, which is the upper (larger- $y$ ) boundary of the region of positive vorticity and is, at the same time, the lower (smaller- $y$ ) boundary of the region of negative vorticity, represents the interjacent line of a pair of vortex motions. These interjacent lines are shown by thick solid lines in figure 10.

There are other zero-vorticity lines that are the upper boundary of the negative vorticity region and are, at the same time, the lower boundary of the positive

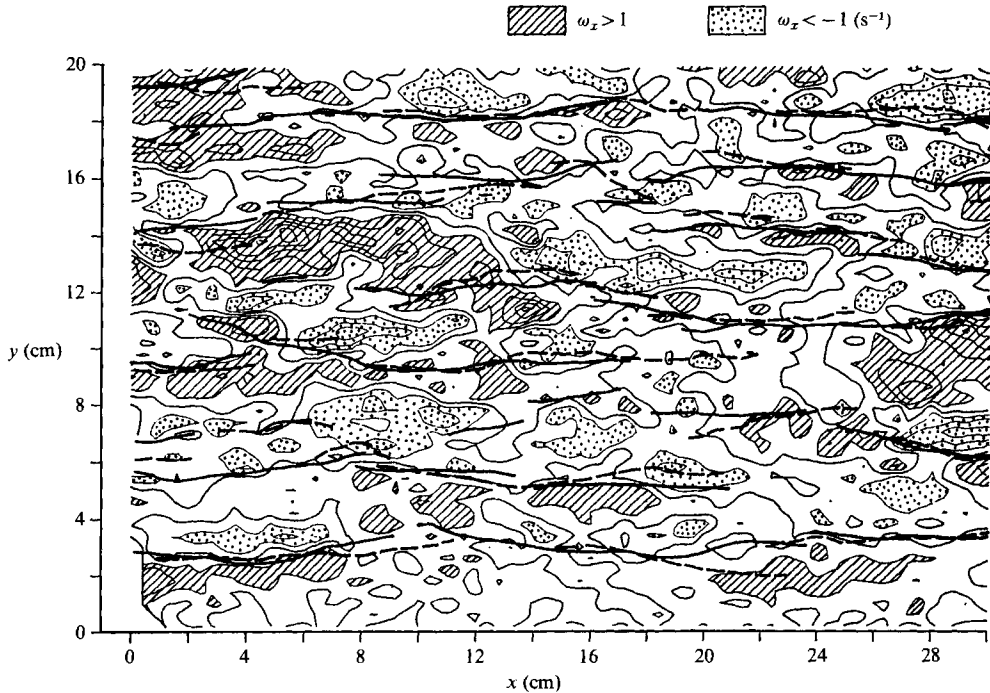


FIGURE 28. Distribution of the streamwise component of vorticity in the cross-section between cross-sections 234 and 235.

vorticity region. These lines pass through the high-speed regions of velocity  $u$ . For convenience, we call these two kinds of lines interjacent and high-speed lines. Most regions with large absolute values for the  $z$ -component of vorticity are close to the interjacent lines and somewhat distant from the high-speed lines. But there are some places [e.g. (14, 11 cm), (16, 14 cm), (16, 18 cm), (10, 8 cm) and (1, 16 cm) in figure 10*a*] where regions of large absolute vorticity values with different signs are close together on the high-speed line; here, sweeps are strong as shown in figure 27.

(ii) *Distribution of the streamwise component of vorticity*

The distribution of the streamwise component of the vorticity vectors  $\omega_x$  in the horizontal cross-section was calculated and is shown in figure 28. Here,  $\partial v/\partial z$  was obtained from the vertical difference in velocity components between the upper and lower cross-sections which are vertically 5.3 mm (31 viscous length) apart. But  $\partial w/\partial y$  was calculated from the distribution of  $w$  in cross-section 235. Accordingly, the distribution obtained for the  $x$ -component of the vorticity  $\omega_x$  does not have good resolution and should be interpreted as being the distribution in the horizontal cross-section between cross-sections 234 and 235.

Interjacent lines in cross-section 234, which are given in figure 10(*b*), are shown by solid lines in figure 28 and those in 235, which are given in figure 10(*a*), by broken lines. If an individual vortex motion has a smooth configuration with its head raised in the streamwise direction, the regions of positive  $\omega_x$  and  $\omega_z$  must nearly coincide, as must the regions of negative  $\omega_x$  and  $\omega_z$ . Actually, many of the positive regions of  $\omega_x$  are located just below (smaller- $y$ ) the interjacent line and the negative regions just above (larger- $y$ ) them. That is the same tendency as for the distribution of  $\omega_z$ .

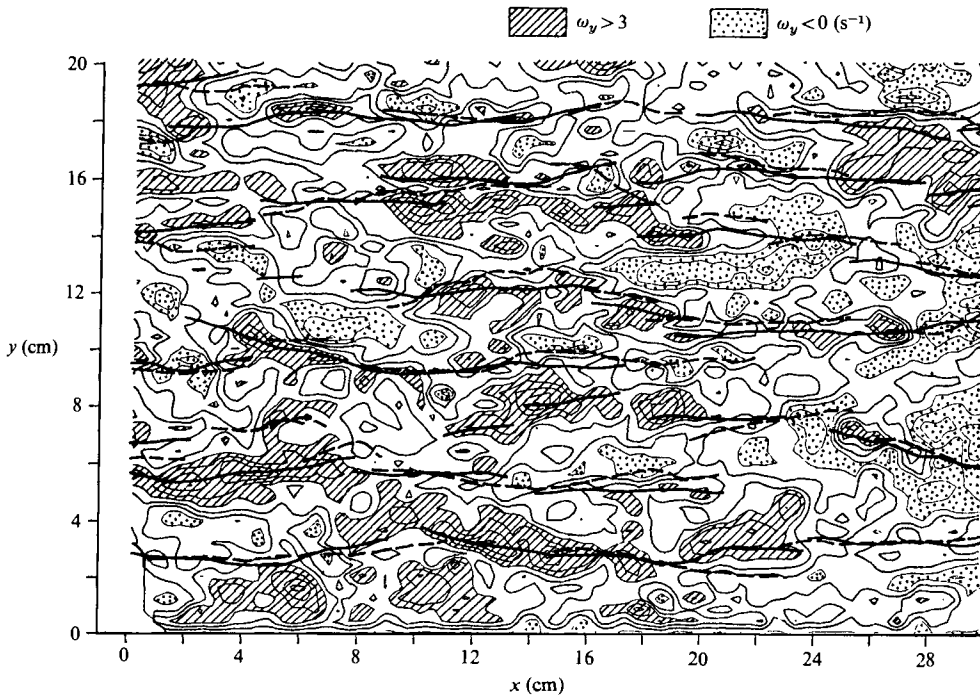


FIGURE 29. Distribution of the spanwise component of vorticity in the cross-section between cross-sections 234 and 235.

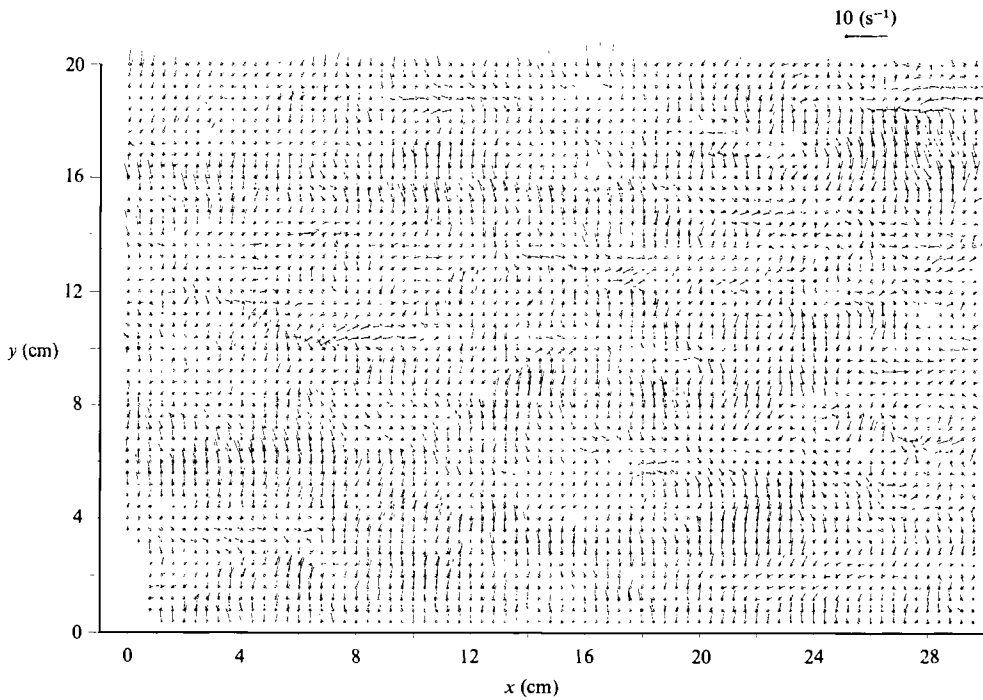


FIGURE 30. Distribution of the horizontal component of vorticity vectors in the cross-section between cross-sections 234 and 235.

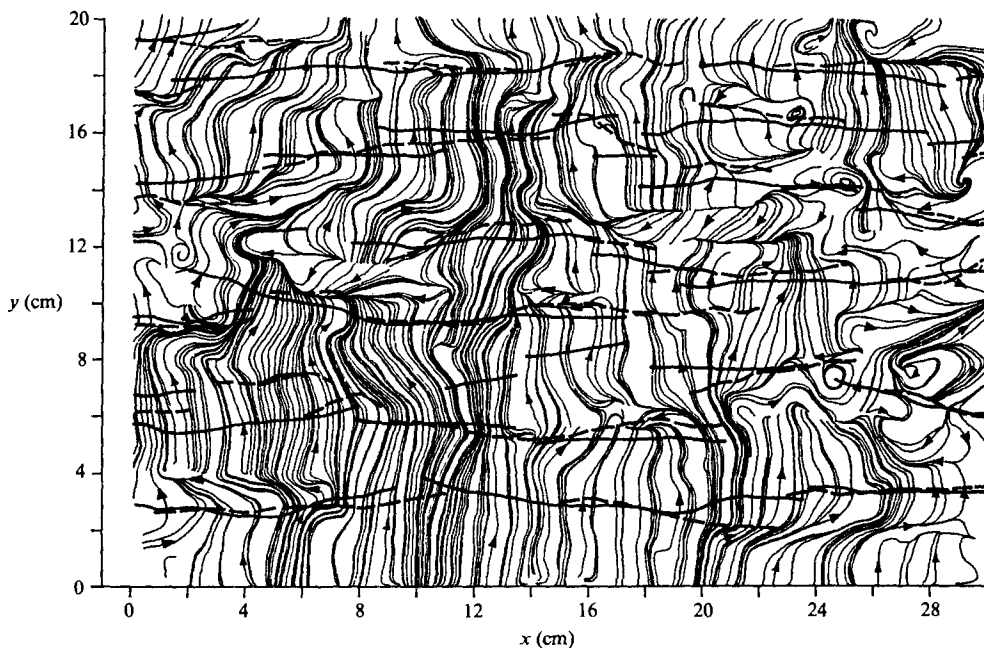


FIGURE 31. Patterns of two-dimensional vortex lines in the cross-section between cross-sections 234 and 235.

(iii) *Distribution of the spanwise component of vorticity*

The distribution of the spanwise component of vorticity  $\omega_y$  in the horizontal cross-section is given in figure 29. The interjacent lines of cross-section 234 are shown by solid lines and of 235 by broken lines. The accuracy of the calculation of the vorticity component is interpreted as being the same as that of the  $x$ -component; but it is apparent that  $\omega_y$ , on the average, is 4 to 5 times as large as the  $x$ -component of vorticity in this cross-section.

This figure shows many interjacent lines passing near the ridge of the  $\omega_y$  distribution, which suggests that every vortex filament that has been loaded with large vorticity near the wall is raised upward near the interjacent lines. It is noted that the large peak value of  $\omega_y$  is located near the upstream end of the interjacent lines, which suggests the existence of the localized free-shear layer observed by Corino & Brodsky (1969) and by Blackwelder & Eckelmann (1979).

(iv) *Patterns of two-dimensional vortex lines*

The distribution of the horizontal component of the vorticity vectors in the horizontal cross-section, which is defined as  $\omega_x \cdot \mathbf{i} + \omega_y \cdot \mathbf{j}$  (where  $\mathbf{i}$  is the unit vector in the streamwise direction and  $\mathbf{j}$  that in the spanwise direction), is shown in figure 30. Patterns of two-dimensional vortex lines obtained by drawing curves tangential to the horizontal component of vorticity vectors are shown in figure 31. Interjacent lines also are drawn in this figure; but because it is the horizontal cross-section of the flow field, we cannot display the three-dimensional configurations of the vortex lines as Moin & Kim (1985) did. Two-dimensional vortex lines are seen convex to the streamwise direction near the interjacent lines, indicative of the existence of horseshoe vortices with their heads raised near those lines.

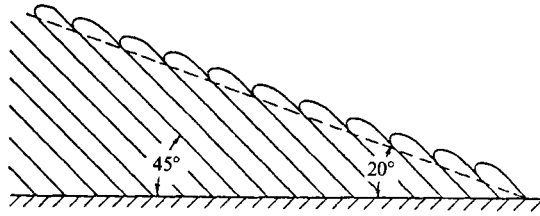


FIGURE 32. Side view of a drawing of a turbulence structure showing double-structure characteristics, by Head & Bandyopadhyay (1981).

## 6. Discussion

An integrated examination of the results of our analyses convinced us that the elementary unit of the coherent structure of turbulent flow near the wall is a horseshoe vortex with two legs. The horizontal cross-section of the right leg (facing streamwise) has generally positive  $x$ - and  $z$ -components of vorticity and the horizontal cross-section of the left leg has negative ones.

### 6.1. Characteristics of the double structure of turbulence

In §4.5 we obtained  $19.2^\circ$  as the average inclination angle of turbulence structures from the phase lag of the  $u$ -fluctuations between cross-sections 234 and 235, and  $36.0^\circ$  from that of the vorticity fluctuations. This appears to be contradictory, but brings to mind the conceptual model proposed by Head & Bandyopadhyay (1978, 1981) suggesting the double structure of turbulence which has two characteristic angles.

Head & Bandyopadhyay provided the conceptual picture of the turbulence structure shown in figure 32 based on measurements with hot wires and flow visualization over the entire widths of turbulent boundary layers. They explained the existence of small-scale hairpin vortices on the upstream face of the large-scale motion and showed that individual hairpin vortices incline to the wall at a characteristic angle ( $45^\circ$ ) and that their tips lie on a line that makes a smaller angle than the individual vortex. Smith (1984) proposed a similar model for the turbulence structures in the near-wall region using flow visualization of open-channel flow, in which individual hairpin vortices make an average angle of  $45^\circ$  with the wall surface and the tips of these vortices are aligned on a line with an angle of  $15^\circ$ – $30^\circ$  to the wall surface. It is noted that the two angles determined by Head & Bandyopadhyay through the measurement across the entire widths of boundary layers and those by Smith through flow visualization of an inner region nearly coincide respectively. Their hairpin vortex is thought to correspond to our horseshoe vortex.

The correlation coefficient of the  $u$ -fluctuation, which has been defined in the preceding section, does not always reflect the characteristics of an individual vortex; it depends on the whole structure of a group of vortices because the velocity field is determined by the integrated forces of individual vortices on the bases of the Biot–Savart law. Consequently, the angle obtained from the phase lag of the  $u$ -fluctuation does not give the average inclination of an individual vortex, but rather the average inclination of the large-scale motion of turbulence.

In fact, the inclination angle of  $18^\circ$ , obtained by Brown & Thomas (1977) through correlation analysis of  $u$ -fluctuations is in good agreement with the outline of a smoke picture visualized by Falco (1977). Kreplin & Eckelmann (1979) showed that the front of the turbulence structure makes an angle of  $4.7^\circ$  with the wall in the viscous

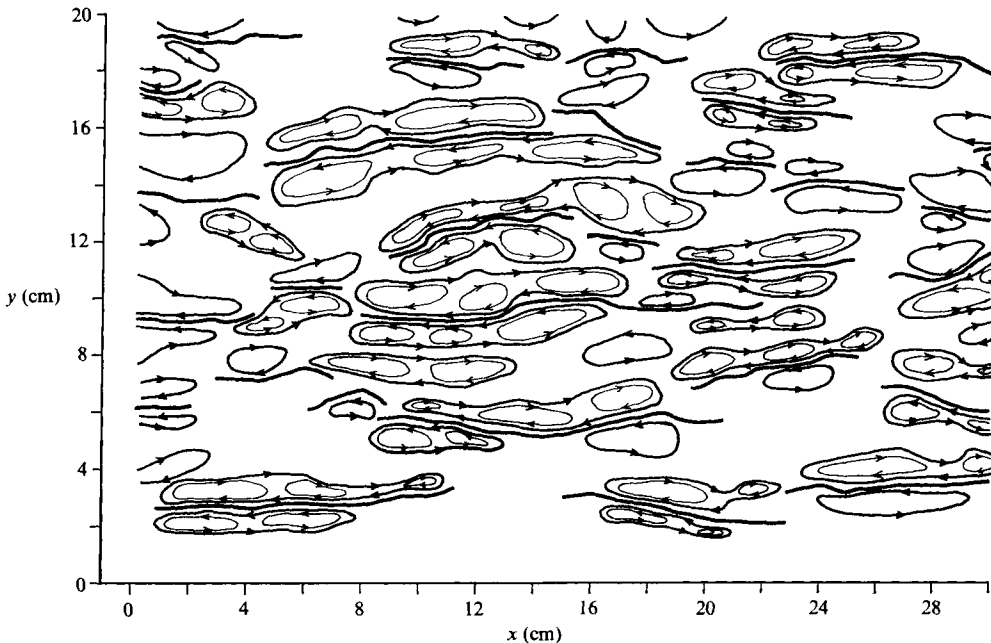


FIGURE 33. Arrangement of cross-sections of horseshoe vortices (fine solid lines with arrows showing the direction of rotation), large-scale vortex motions (thick solid lines with arrows) and interjacent lines (thick solid line) (cross-section 235).

sublayer ( $z^+ \leq 5$ ) and the angle increases with the distance from the wall to the value of  $10^\circ$ – $15^\circ$  at the height of  $z^+ = 40$ , which is nearly equal to the height of our observation. Nakagawa & Nezu (1981) determined the angle of the maximum correlation line to the wall surface to be  $15^\circ$ – $20^\circ$  through the space-time-correlation analysis of  $u$ -fluctuations obtained by hot-film measurement for the turbulence structure in the near-wall region in open-channel flow. These angles nearly coincide with the angle of  $19.2^\circ$  obtained through our correlation analysis of  $u$ -fluctuations.

By contrast, it is natural to think that the inclination angle of  $36^\circ$  obtained through our vorticity-correlation analysis gives the average inclination angle of an individual vortex because vorticity fluctuations are believed to correspond to individual vortices. This angle is nearly equal to that presented by Head & Bandyopadhyay and Smith.

Concerning the distribution of the  $z$ -component of vorticity (figures 10*a*, *b*), the areas with large, absolute vorticity values (areas in which  $|\omega_z| > 1.0$  ( $\text{s}^{-1}$ )) are shown by hatching or dotting) stretch in a streamwise direction and contain from one to four peaks of vorticity, which also suggests a double structure of turbulence: the areas with large absolute vorticity values correspond to large-scale vortex motion and each local peak of vorticity to the centre of an individual horseshoe vortex. Therefore, the double structure of turbulence is shown by our visualization data also.

Around the centre of an individual cross-section of a horseshoe vortex, the vorticity must be concentrated and, at the same time, streamline patterns must be focal, spiral or wavy when the flow field is observed from a reference frame moving at a velocity just, or nearly, equal to that at the point. We have established a practical arrangement for the cross-sections of vortex motions in cross-section 235 (shown in

figure 33) based on our conceptual model of the double structure of turbulence, the distribution of vorticity (figure 10*a*) and the patterns of streamlines (figures 9*a*, *b*).

In figure 33, the areas enclosed by fine solid lines show the posited cross-sections of the legs of horseshoe vortices. These lines were drawn to encircle the local peak of vorticity distribution around which streamlines have the characteristic patterns described. Arrows denote the direction of rotation.

The cross-sections of the large-scale vortex motions are drawn with thick, solid lines that are nearly the same as the  $\pm 1.0$  ( $\text{s}^{-1}$ ) contour lines of the  $z$ -component of vorticity. The axes of the large-scale vortex motions make a smaller angle with the wall than that of horseshoe vortices and so the horizontal cross-section of large-scale vortex motions are stretched in the flow direction. These large-scale vortex motions are considered equivalent to what Blackwelder & Eckelmann (1979) called a longitudinal vortex, and so we shall call them longitudinal vortices hereafter. Generally, each cross-section of a longitudinal vortex contains a few cross-sections of horseshoe vortices. In some cases, a horseshoe vortex exists alone. Most longitudinal vortices have counterparts with the opposite sign of vorticity as pointed out by Blackwelder & Eckelmann.

The number of horseshoe vortices found to compose a longitudinal vortex is close to that reported by Smith (1983), who used the hydrogen-bubble method for open-channel flow. Head & Bandyopadhyay (1981) reported that the arrangements and configurations of horseshoe vortices depend on the Reynolds number. Note that our reported arrangement of vortex motions is that existing under flow conditions with a Reynolds number of 2600.

### 6.2. The scale of turbulence structures

In § 4 we reported that the average characteristic scale of  $u$ -fluctuation, which nearly corresponds to a quarter of a wavelength, is about 7.9 cm and that of  $v$ -fluctuations 3.7 cm. The problem remains of why the scale of  $u$ -fluctuation differs from that of  $v$ -fluctuation and which denotes the true scale of the turbulence structure.

In figure 34, the lines of the zero autocorrelation coefficient of the  $u$ -fluctuation in figure 21 are shown by solid lines and those of the  $v$ -fluctuations in figure 22 by broken lines. In this figure two kinds of ranges can be distinguished: range A, in which  $y = 2-3$ , 5.5-6.5, and 13.5-20 cm; and range B, in which  $y = 3-5.5$ , 6.5-13.5 cm.

In the A-range, the average  $x'$ -coordinate, about 5 cm, of the zero-crossing of the correlation coefficients of  $u$ -fluctuation is nearly equal to that of the  $v$ -fluctuation; accordingly, the wavelengths of the  $u$ - and  $v$ -fluctuations are both about 20 cm. By contrast, in the B-range,  $x'$ -coordinates of the zero-crossing of the correlation coefficient of the  $v$ -fluctuation are about 2.5 cm; accordingly, the wavelength of the  $v$ -fluctuation is about 10 cm. But, in the B-range, the wavelength of the  $u$ -fluctuation is much larger and more variable.

This suggests that turbulence structures have a unit structure with a characteristic scale of about 10 cm and the wavelength of velocity fluctuations is determined by the arrangement of the unit structures. Note that this scale, 10 cm, is nearly equal to the average scale of the longitudinal vortex shown in figure 33. Therefore, the unit structure which determines the wavelength of velocity fluctuations is considered to be a longitudinal vortex.

The practical arrangement of the cross-sections of longitudinal vortices in figure 33 show that there are a few typical arrangements (figure 35). Type A (figure 35*a*) is the most typical type of arrangement in which longitudinal vortices are arranged

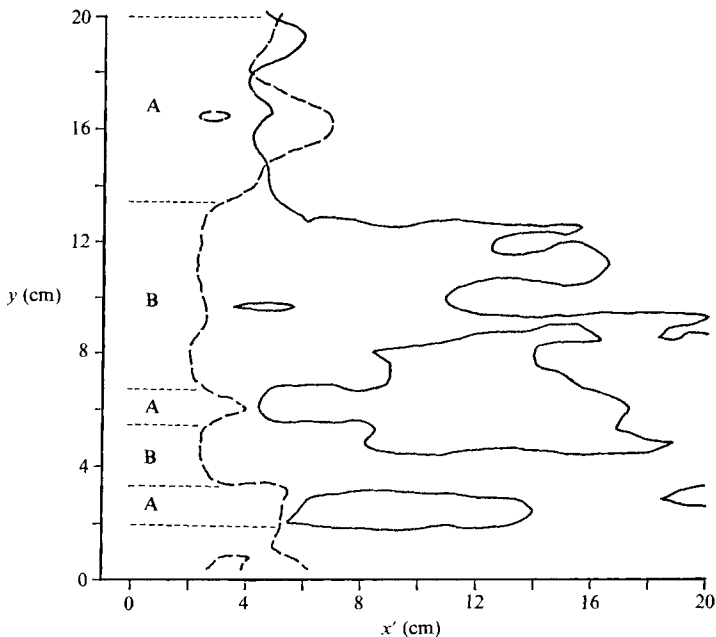


FIGURE 34. Lines of zero autocorrelation coefficient for the  $u$ -fluctuation (solid lines) and the  $v$ -fluctuation (broken lines).

in a staggered array. In type B, groups of longitudinal vortices are arranged in a staggered array, each group being composed of  $n$  longitudinal vortices arranged on a line. The case of  $n = 3$  is shown in figure 35(b). When  $n = 1$ , type A coincides with type B. Type C is the case when the type-A arrangement is somewhat distorted in the spanwise direction. For simplicity, we assume that the cross-sections of the longitudinal vortices are nearly equal in shape and scale (the streamwise scale is denoted by  $d$ ) and that the structure of turbulence is frozen and convected at the velocity  $U_c$ .

Using these simplifying assumptions, we obtain results from probe measurements at a fixed point for two components of velocity. A velocimeter measures the distributions of  $u$  and  $v$  (e.g. on the line shown in figure 35), the variation of the sign of the measured velocity components  $u$  and  $v$  being shown at the bottom of each figure. The wavelengths  $\lambda_u$  and  $\lambda_v$  of the  $u$ - and  $v$ -fluctuations obtained through autocorrelation analysis are evaluated as the average length of a combination of series of positive and of negative signs, and are shown at the bottom of the figure.

In cases of the A-type we get  $\lambda_u = 2d$  and  $\lambda_v = 2d$  and in the B-type,  $\lambda_u = 2nd$  and  $\lambda_v = 2nd/(2n-1)$ . In the latter type, the wavelength of the  $u$ -fluctuation  $\lambda_u$  varies with  $n$ , but the wavelength of the  $v$ -fluctuation  $\lambda_v$  is almost constant and nearly equal to  $d$  when  $n$  is larger than 2. In the case of type C,  $\lambda_u = 4d$  and  $\lambda_v$  is nearly equal to  $d$ . This suggests that in the A-range of figure 34, the vortices are arranged in the A-type and, in the B-range, the arrangement in the region near the sidewall is of the B-type, and that far from the sidewall of the C-type.

Our conclusions about the scale of turbulence structures and the method of measuring them are: (i) The wavelength  $\lambda_u$  of the  $u$ -fluctuations obtained through autocorrelation analysis of velocity data by fixed-point measurement sometimes differs from the wavelength  $\lambda_v$  of the  $v$ -fluctuation obtained by the same method

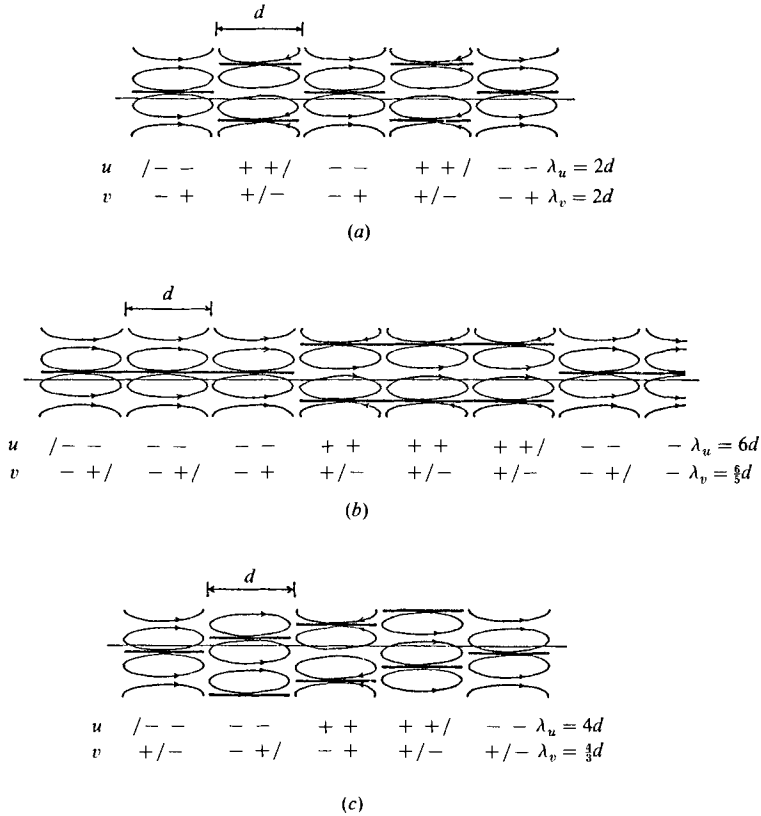


FIGURE 35. Typical arrangements of cross-sections of longitudinal vortices (solid lines with arrows showing the direction of rotation) and scale estimation of  $u$ - and  $v$ -fluctuation in the horizontal cross-section of the flow. (a) Type A; (b) type B; (c) type C.

during the same interval. (ii) The wavelength  $\lambda_u$  does not always reflect the true lengthscale of a turbulence structure; it depends on the arrangement of the longitudinal vortices. (iii) But, the wavelength  $\lambda_v$  generally reflects the lengthscale of a turbulence structure,  $\lambda_v$  being equal to  $d$  (in the B-range) or to  $2d$  (in the A-range). (iv) Therefore, it is better to use the  $v$ -data to determine the scale of the longitudinal vortex through correlation analysis. (v) Note that the above discussion is based on data for a short period. If we use sufficiently long-time data, in which the arrangement of turbulence structure of A-, B- and C-type will be contained, we shall obtain a value between  $d$  and  $2d$  for an average wavelength of  $v$ -fluctuation. It is important to determine the appropriate sampling period for the fixed-point measurement.

Clearly, from the above estimation of the A-type of arrangement, the average streamwise scale of a longitudinal vortex  $d$  is half the average wavelength, estimated as 20 cm from figure 34. Therefore, the average streamwise scale of a longitudinal vortex  $d$  is 10 cm in a cross-section of  $z = 9.3$  mm, a scale of the order of  $600 \nu/u_*$  at  $zu_*/\nu = 56.3$ . Actually, in figure 33, the streamwise scale of a longitudinal vortex is distributed between 4 and 14 cm, the average being about 10 cm. It should be noted that above-stated scale of longitudinal vortex is that of the horizontal cross-section of the vortex, and the length of axis of the vortex is far larger. In Kreplin & Eckelmann (1979) it is about  $1200 \nu/u_*$ .

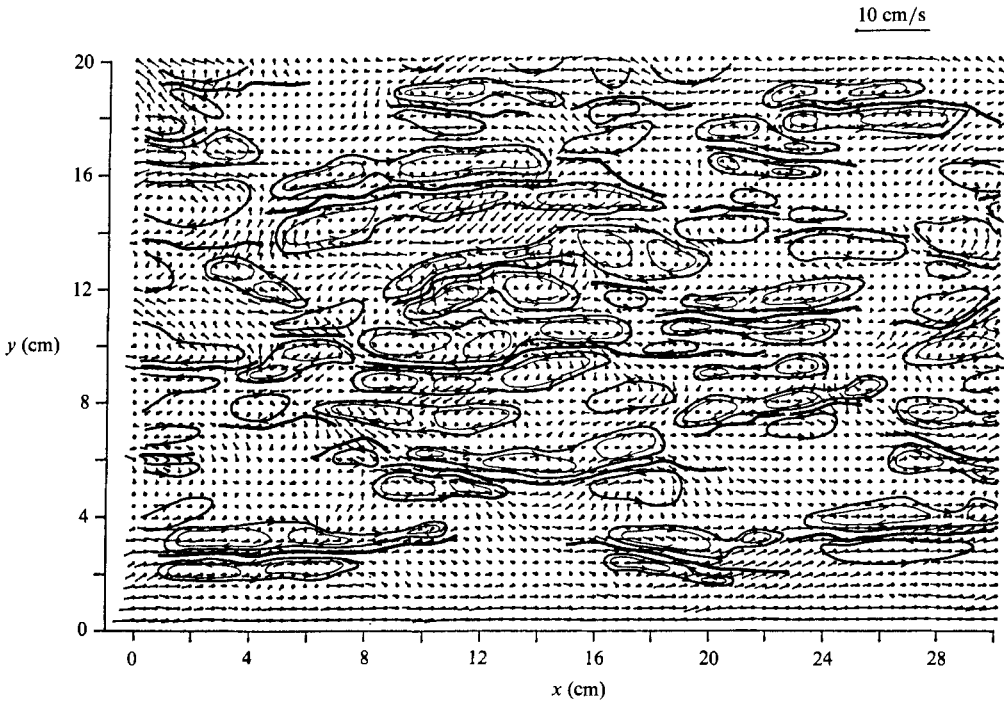


FIGURE 36. Arrangement of the double structure of vortex motion superposed on the distribution of velocity vectors (cross-section 235).

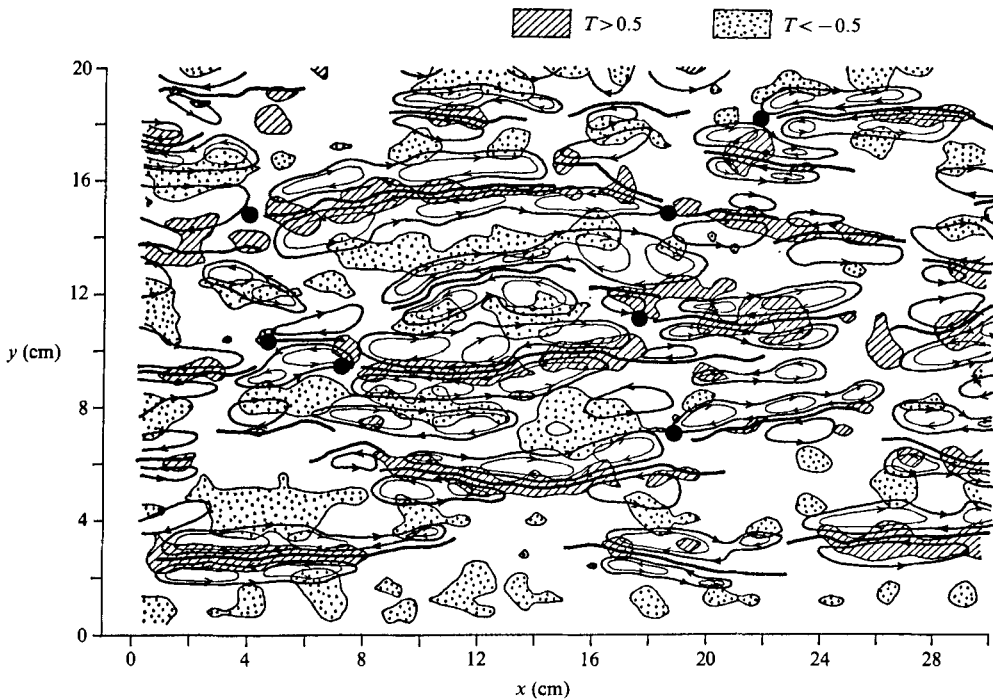


FIGURE 37. Arrangement of the double structure of vortex motion, interjacent lines (thick solid lines), ejections (hatched area) and sweeps (dotted area) (cross-section 235). Large dots represent the localized acceleration regions.

By contrast, the streamwise scale of an individual horseshoe vortex is 3–5 cm, that is  $180\text{--}300 \nu/u_*$ . Cantwell (1981) summarized the average scales of various vortices and reported that the longitudinal scale of outer-flow vortices is of the order of  $200 \nu/u_*$ . But, in the distribution of the  $z$ -component of vorticity (figure 10), we counted an average of 10–11 legs of longitudinal vortices in the spanwise interval  $y = 3\text{--}20$  cm. Therefore, we estimated the average spanwise scale of a longitudinal vortex as 1.6 cm, that is of the order of  $100 \nu/u_*$ .

### 6.3. Streak structures, ejections and sweeps

Figure 36 shows the distribution of the velocity vectors shown in figure 6 superposed on the arrangement of double-structural vortex motions (figure 33). In this figure, the mean streamwise velocity in the cross-section is subtracted from each velocity vector. Therefore, the low-speed region is the region in which velocity vectors point in the upstreamwise direction, and in the high-speed region they point downstream. Low-speed regions are located between two legs of a pair of longitudinal vortices and high-speed regions between two neighbouring pairs of longitudinal vortices.

As stated, the area of ejection in the horizontal cross-section of the flow field is shown by the area of positive  $T$ -function (figure 27), the area of sweep by the area of negative  $T$ -function and the magnitude of the ejection or sweep is given by the absolute value of the  $T$ -function. The range in which the  $T$ -function has an absolute value larger than 0.5 is shown in figure 37, on which the arrangement of the double-structural vortex motions in figure 33 is superimposed. This figure clearly shows that ejections are generated in the narrow region between the two legs of a horseshoe vortex and that sweeps are generated between two pairs of longitudinal vortices.

### 6.4. Characteristics of the localized accelerating region

The conditional-sampling techniques used for probe measurements have made an important contribution to the determination of the coherent structure of turbulence. In data analysis using conditional-sampling techniques, special attention has been paid to the localized accelerating region of the probe-measurement data. We here examine the structural features in, and around, the region and discuss the VITA technique using our flow-visualization data.

Localized accelerating regions are found in the distribution of the  $x$ -component of velocity (figure 7) around the points (5, 10 cm), (4, 15 cm), (7, 9 cm), (18, 11 cm), (19, 7 cm), (19, 15 cm) and (22, 18 cm). As an example, we shall examine the distributions of  $u$  and  $w$  around the point (18, 11 cm). The longitudinal distributions of  $u$  and  $w$  on the lines  $y = 11.5, 11.25, 11.0, 10.75$  and  $10.5$  cm in the horizontal cross-section 235 are given in figure 38. Note that  $u$  decelerates in the  $x$ -direction around point (18, 11 cm), and around that point  $w$  generally is of opposite sign to  $u$ .

If we measure the  $u$ - and  $w$ -fluctuations at a fixed point by the probe method, and assume that the velocity distribution is frozen in the horizontal cross-section, the configuration of the velocity fluctuation in figure 38 is obtained, but the abscissa  $x$  is replaced by  $t$ , denoting time, in the direction opposite to that of  $x$ . The configurations of the  $u$ - and  $w$ -fluctuation obtained are analogous to the typical  $u$ - and  $w$ -fluctuation patterns with the passage of time obtained through the VITA technique by Blackwelder & Kaplan (1976) and by Johansson & Alfredsson (1982) and through the pattern-recognition technique by Wallace, Brodkey & Eckelmann

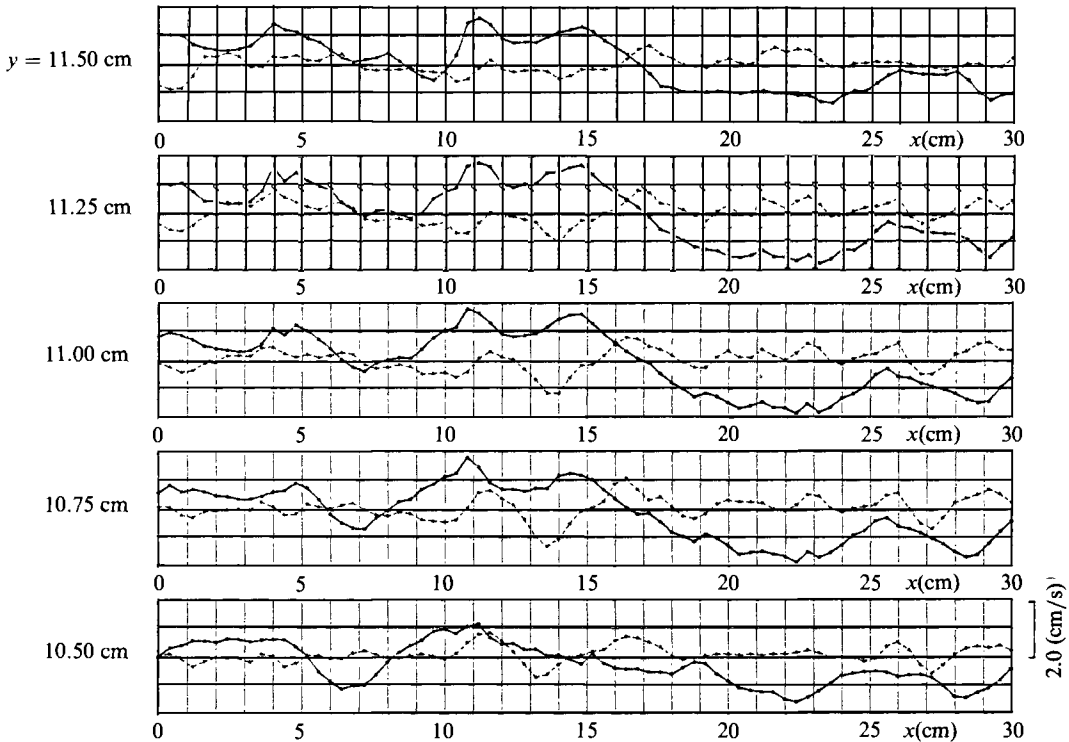


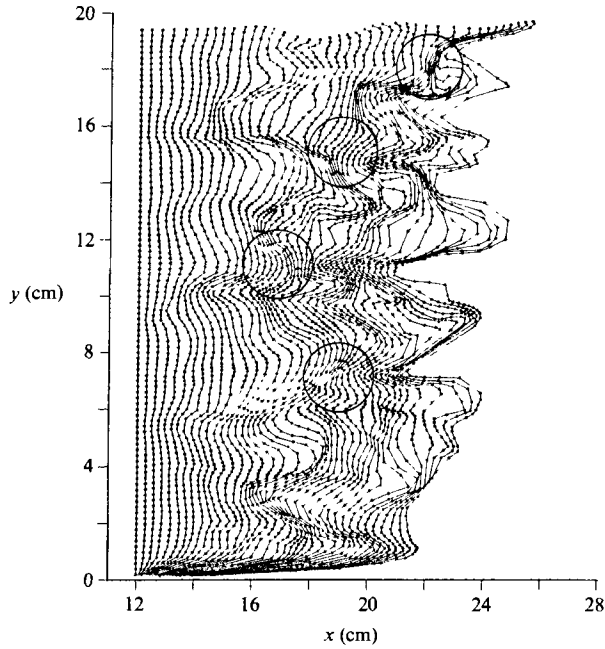
FIGURE 38. Longitudinal distribution of  $u$  (solid line) and  $w$  (broken line) on the lines  $y = 10.5$ ,  $10.75$ ,  $11.0$ ,  $11.25$  and  $11.5$  cm (cross-section 235).

(1977). Thus, the local flow patterns that we are concerned with are the patterns detected through the VITA and pattern-recognition techniques.

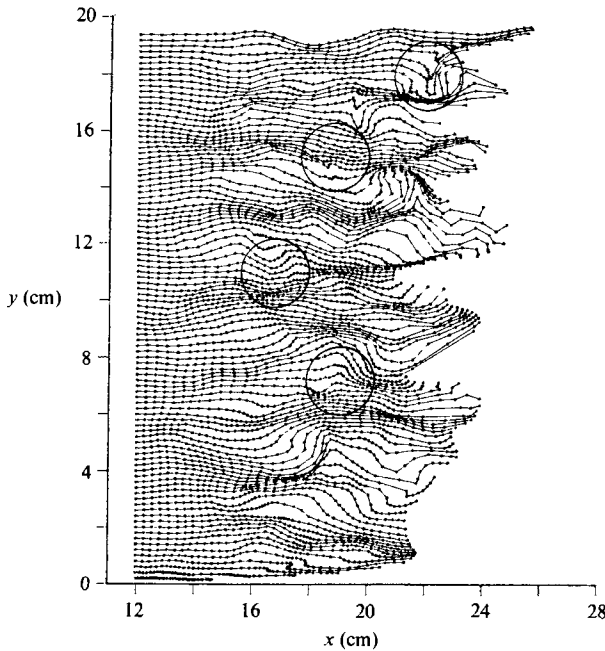
The location of the above seven points are plotted in figure 37 which shows the arrangements of horseshoe vortices and of ejections and sweeps. All seven points, denoted by large dots, are upstream end points of interjacent lines. Note that in figure 37 strong ejections exist at locations just downstream of these points, which coincides with Tiederman's statement (see the discussion in Kunen, Ooms & Vink 1984) that the VITA technique captures acceleration events that occur at the ends of bursts.

By contrast, figure 37 shows that there are strong sweep regions upstream of the point in question. Individual sweep regions, however, are arranged somewhat irregularly with respect to this point; some are fairly far from the point, some are near it and some are slantingly upstream of it. If the VITA technique is applied to such a flow, ejection events should be detected clearly, but the sweep not so clearly because of the cancelling in the process of ensemble averaging. Actually, in the experimental study by Alfredsson & Johansson (1984), the contribution of sweep events to Reynolds stress was not revealed using the VITA technique.

Hama & Nutant (1963) introduced a hydrogen-bubble method with which they observed the transition mechanism. Since then, there have been a number of studies using the hydrogen-bubble method that have revealed the coherent structure of turbulence [e.g. Kline *et al.* 1967; Kim, Kline & Reynolds 1971; Offen & Kline 1974; Grass 1971; Smith 1978, 1984]. Through these studies some typical patterns of



(a)



(b)

FIGURE 39. Hydrogen-bubble-line patterns calculated using visualization data on the assumption of frozen turbulence. Localized free-shear layers occur within the encircled regions. (a) Timelines; (b) streaklines.

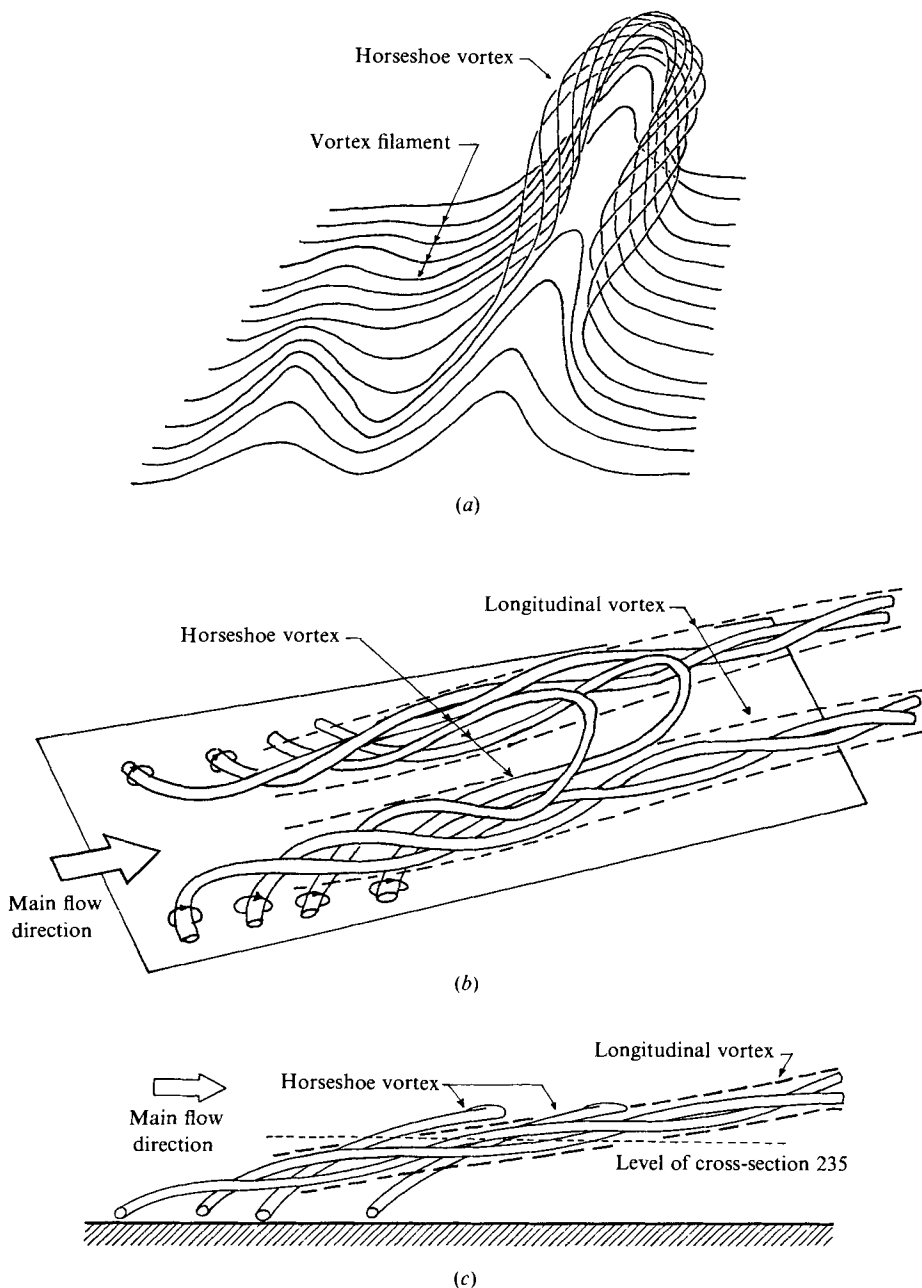


FIGURE 40. Conceptual model representing (a) the formation and developing stages of a horseshoe vortex, (b) the overall structure of turbulence in the wall region in the fully developed stage, and (c) the side view. Solid lines denote vortex filaments in (a) and tubes in (b) and (c), horseshoe vortices.

hydrogen-bubble tracers showing the coherent structure of turbulence have been obtained.

What pattern of hydrogen-bubble tracers would appear if this method were applied to the flow that we have examined? Timelines and streaklines, calculated on the assumption that the velocity distribution in the horizontal cross-section is frozen and

the bubble-generating electrode is placed at  $x = 12$  cm in horizontal cross-section 235, are given in figures 39(*a*, *b*). Low-speed and high-speed regions clearly are generated. These regions coincide with those in figure 7 which gives the distribution of the  $x$ -component of velocity. In this figure, four of the seven points representing the localized accelerating regions are visible and are enclosed by circles. The timelines are grouped very closely around these points because of localized deceleration in the  $x$ -direction.

### 6.5. Conceptual model of the coherent structure of turbulence

We propose a conceptual model of the coherent structure of turbulence based on the results presented here. A turbulent open-channel flow is characterized by the existence of a high-shear layer (viscous sublayer) with high vorticity near the channel bed. If disturbances are experienced by part of it, the high-shear layer will be deformed slightly into wavy patterns, and the existing vorticity will be concentrated locally. Once local concentrations of vorticity are formed, they entrain the nearby vortex filaments in the sublayer and become stronger. At the same time, they are lifted up (Biot–Savart law) and elongated by mean flow. Thus, the high vorticity originating in the sublayer is organized to form a horseshoe vortex in the buffer layer. In the sublayer very close to the wall, the flow structure is almost two-dimensional and the existing large vorticity does not form a vortex. A conceptualized picture of a horseshoe vortex in its formation stage is given in figure 40(*a*), in which vortex filaments are denoted by solid lines.

A horseshoe vortex is stretched by the main flow and, at the same time, entrains others, as well as vortex filaments. A newly entrained horseshoe vortex is also stretched by the main flow and spirals around an original horseshoe vortex. This process is repeated again and again and horseshoe vortices are organized to form a larger-scale vortex motion. The conceptualized three-dimensional configurations and the side view of the organized vortex motions in the fully developed stage are shown in figures 40(*b*, *c*) in which horseshoe vortices are denoted by vortex tubes. The upper part of the organized horseshoe vortices forms a bundle of spiral vortex tubes, as shown by the broken lines in the figure. It is this bundle of vortex tubes that we have described as a longitudinal vortex. As stated, longitudinal vortices generally have counterparts with the opposite sign of vorticity. But horseshoe vortices do not always have a counterpart because they are deformed in the process of the entrainment.

Our conceptual model is composed of three phases of vortex motions: vortex filaments, horseshoe vortices and longitudinal vortices. Through the above-stated process, these vortices are deformed and stretched, which is also the process of energy dissipation.

In our conceptual model, in the buffer layer the axes of the horseshoe vortices entrained in the longitudinal vortex are not parallel to the axis of the longitudinal vortex, rather they spiral around the axis. In particular, in the narrow regions interjacent between the two legs of a pair of longitudinal vortices, the axes of horseshoe vortices form large angles with the wall surface as shown in figure 40(*c*). Consequently, the fluid in the interjacent region is driven in the upstream, upward direction (Biot–Savart law). This is the mechanism for upward and upstream motion in the ejection region. In a region surrounded by two pairs of longitudinal vortices, the fluid is driven downward and downstream (Biot–Savart law); this is the generating mechanism of sweeps.

Once sweeps occur, a thin but high-shear layer is formed locally over the wall surface. This high-shear layer will trigger the new series of vortex formation described

above. The strong upward motion near the upstream end of the organized vortex motions lifts the high-shear layer, giving rise to a localized free-shear layer and an inflexional distribution of velocity.

As a result, this generating mechanism organizes a staggered arrangement of longitudinal vortex motions. The staggered pattern observed by Falco (1981), who used flow visualization by smoke, is believed to be this stage of development in turbulence structures. His tracer is believed to have flown near the wall with the result that the flow structures around the roots of the longitudinal vortex motions are clearly visualized. Therefore, the vortex model proposed by Falco is believed to represent the effect of the right leg (facing streamward) of a pair of longitudinal vortices and the left leg of another pair. He also proposed a pocket surrounded by these vortices, which must be the visualized sweep whose generating mechanism is given above.

The level of cross-section 235 is shown by the broken line in figure 40(c). Our conceptual model shows that the horizontal cross-section of a longitudinal vortex contains some cross-sections of horseshoe vortices. That is the reason why the distribution of the vertical component of velocity along the interjacent line is wavy as shown in figure 38.

By combining the results obtained by correlation analysis with this conceptual model of turbulence structure, we obtain quantitative information about organized vortex motions. The average streamwise scale of the cross-sections of longitudinal vortices is 10 cm ( $600 \nu/u_*$ ), and the spanwise scale is 1.6 cm ( $100 \nu/u_*$ ). The streamwise scale of an individual horseshoe vortex is 3–5 cm, that is  $180\text{--}300 \nu/u_*$ . Longitudinal vortices, on average, make an angle of  $19^\circ$  with the wall. By contrast, horseshoe vortices make an angle of  $36^\circ$ .

Our proposed model of the coherent structure of turbulence has the following characteristics: (i) It is a multi-layered structure. In the sublayer, there is a high-shear layer that is almost two-dimensional. In the buffer layer, the axes of the horseshoe vortices spiral around the axis of the longitudinal vortex generating three-dimensional, complex flow patterns such as ejections, sweeps and localized free-shear layers. (ii) It has characteristics of a multiple structure. Vortex filaments of fine scale are organized to form a horseshoe vortex, and one or more horseshoe vortices make longitudinal vortex. (iii) Order is coexistent with disorder. There is some order in the mechanism of vortex formation, in the arrangement of vortices and in their scale distribution, some of which is revealed; but, there is also disorder in every part. (iv) It is self-conserving of its coherent structure. The energy in the mean flow is given to coherent structures through sweeps driven by existing longitudinal vortex motions. These sweeps give rise to new series of organized vortex motions.

We thank Professor H. Imamoto and Dr R. Kinoshita for their most helpful advice about and encouragement of our investigations.

#### REFERENCES

- ALFREDSSON, P. H. & JOHANSSON, A. V. 1984 On the detection of turbulence-generating events. *J. Fluid Mech.* **139**, 325.
- BLACKWELDER, R. F. & ECKELMANN, H. 1979 Streamwise vortices associated with the bursting phenomenon. *J. Fluid Mech.* **94**, 577.
- BLACKWELDER, R. F. & KAPLAN, R. E. 1976 On the wall structure of the turbulent boundary layer. *J. Fluid Mech.* **76**, 89.

- BROWAND, W. & WEIDMAN, P. D. 1976 Large scales in the developing mixing layer. *J. Fluid Mech.* **76**, 127.
- BROWN, G. L. & THOMAS, A. S. W. 1977 Large structure in a turbulent boundary layer. *Phys. Fluids* **20**, 243.
- CANTWELL, B. J. 1981 Organized motion in turbulent flow. *Ann. Rev. Fluid Mech.* **13**, 457.
- CORINO, E. R. & BRODKEY, R. S. 1969 A visual investigation of the wall region in turbulent flow. *J. Fluid Mech.* **37**, 1.
- CORRSIN, S. 1957 Some current problems in turbulent shear flows. In *Proc. Symp. Naval Hydrodyn., Publ.* 515, p. 373. Nat. Acad. Sci., Nat. Res. Council.
- FALCO, R. E. 1977 Coherent motions in the outer region of turbulent boundary layers. *Phys. Fluids* **20**, 124.
- FALCO, R. E. 1981 Structural aspects of turbulence in boundary layer flows. In *Proc. 6th Symp. on Turbulence in Liquids* (ed. G. K. Patterson & J. L. Zakin), p. 1. Dept. of Chem. Engng, University of Missouri-Rolla.
- GRASS, A. J. 1971 Structural features of turbulent flow over smooth and rough boundaries. *J. Fluid Mech.* **50**, 233.
- HAMA, F. R. & NUTANT, J. 1963 Detailed flow field observations in the transition process in a thick boundary layer. In *Proc. Heat Transfer Fluid Mech. Inst.* 77. Stanford University Press.
- HEAD, M. R. & BANDYOPADHYAY, P. 1978 Combined flow visualization and hot wire measurements in turbulent boundary layers. In *Lehigh Workshop on Coherent Structure in Turbulent Boundary Layers* (ed. C. R. Smith & D. E. Abbott), p. 98. Dept. Mech. Engng & Mech., Lehigh University.
- HEAD, M. R. & BANDYOPADHYAY, P. 1981 New aspects of turbulent boundary-layer structure. *J. Fluid Mech.* **107**, 297.
- IMAICHI, K. & OHMI, K. 1983 Numerical processing of flow-visualization pictures – measurement of two-dimensional vortex flow. *J. Fluid Mech.* **129**, 283.
- JOHANSSON, A. V. & ALFREDSSON, P. H. 1982 On the structure of turbulent channel flow. *J. Fluid Mech.* **122**, 295.
- KIM, H. T., KLINE, S. J. & REYNOLDS, W. C. 1971 The production of the wall region in turbulent flow. *J. Fluid Mech.* **50**, 133.
- KINOSHITA, R. 1981 Velocity measurement of river flows and model channel flows by photogrammetry. *J. Flow Visualization Soc. Japan* **1**, 262 (in Japanese).
- KLINE, S. J. 1978 The role of visualization in the study of the structure of the turbulent boundary layer. In *Lehigh Workshop on Coherent Structure of Turbulent Boundary Layers* (ed. C. R. Smith & D. E. Abbott), p. 1. Dept. Mech. Engng & Mech., Lehigh University.
- KLINE, S. J. & FALCO, R. E. 1980 Summary of AFOSR/MSU reserach specialists workshop on coherent structure in turbulent boundary layers. *AFOSR TR-80-0290*, Dept. of Mech. Engng, Michigan State University.
- KLINE, S. J. & RUNSTADLER, P. W. 1959 Some preliminary results of visual studies of the flow model of the wall layers of the turbulent boundary layer. *Trans. ASME E: J. Appl. Mech.* **26**, 166.
- KLINE, S. J., REYNOLDS, W. C., SCHRAUB, F. A. & RUNSTADLER, P. W. 1967 The structure of turbulent boundary layers. *J. Fluid Mech.* **30**, 741.
- KREPLIN, H. P. & ECKELMANN, H. 1979 Propagation of perturbations in the viscous sublayer and adjacent wall region. *J. Fluid Mech.* **95**, 305.
- KUNEN, J. M. G., OOMS, G. & VINK, P. J. J. 1984 On detection methods for coherent structures in turbulent flows. In *Proc. 8th Symp. on Turbulence* (ed. X. B. Reed, G. K. Patterson & J. L. Zakin), p. 37. Dept. Chem. Engng, University of Missouri-Rolla.
- LAUFER, J. 1975 New trends in experimental turbulence research. *Ann. Rev. Fluid Mech.* **7**, 307.
- MOIN, P. & KIM, J. 1985 The structure of the vorticity field in turbulent channel flow. Part 1. Analysis of instantaneous fields and statistical correlations. *J. Fluid Mech.* **155**, 441.
- NAKAGAWA, H. & NEZU, I. 1981 Structure of space-time correlations of bursting phenomena in an open-channel flow. *J. Fluid Mech.* **104**, 1.
- OFFEN, G. R. & KLINE, S. G. 1973 Experiments on the velocity characteristics of 'bursts' and on the interactions between the inner and outer regions of a turbulent boundary layer. *Stanford Univ. Mech. Engng Dept. Rep.* MD-31.

- OFFEN, G. R. & KLINE, S. J. 1974 Combined dye-streak and hydrogen bubble visual observations of a turbulent boundary layer. *J. Fluid Mech.* **62**, 223.
- OHNARI, H., SAGA, T. & SAITO, T. 1985 The structure of streamwise vortex in the inner layer of turbulent channel flow. *Proc. Japan Soc. Civil Engng* **363**, (II-4), 135 (in Japanese).
- SMITH, C. R. 1978 Visualization of turbulent boundary layer structure using a moving hydrogen bubble wire probe. In *Lehigh Workshop on Coherent Structure in Turbulent Boundary Layers* (ed. C. R. Smith & D. E. Abbott), p. 48. Dept. Mech. Engng & Mech., Lehigh University.
- SMITH, C. R. 1984 A synthesized model of the near-wall behavior in turbulent boundary layers. In *Proc. 8th Symp. on Turbulence* (ed. X. B. Reed, G. K. Patterson & J. L. Zakin), p. 299. Dept. Chem. Engng. University of Missouri-Rolla.
- THEODORSEN, T. 1955 The structure of turbulence. In *50 Jahre Grenzschichtforschung* (ed. H. Gortler & W. Tollmien), p. 55. Braunschweig, Vieweg & Sohn.
- UTAMI, T. & UENO, T. 1979 Lagrangian and Eulerian measurement of large scale turbulence by flow visualization techniques. In *Flow Visualization* (ed. T. Asanuma), p. 221. Hemisphere.
- UTAMI, T. & UENO, T. 1984 Visualization and picture processing of turbulent flow. *Exps. Fluids* **2**, 25.
- WALLACE, J. M., BRODKEY, R. S. & ECKELMANN, H. 1977 Pattern-recognized structures in bounded turbulent shear flows. *J. Fluid Mech.* **83**, 673.
- WALLACE, J. M., ECKELMANN, H. & BRODKEY, R. S. 1972 The wall region in turbulent shear flow. *J. Fluid Mech.* **54**, 39.
- WILLIAMS, D. R., FASEL, H. & HAMA F. R. 1984 Experimental determination of the three-dimensional vorticity field in the boundary-layer transition process. *J. Fluid Mech.* **149**, 179.
- WILLMARTH, W. W. 1975 Structure of turbulence in boundary layers. *Adv. Appl. Mech.* **15**, 159.